

# Development and validation of precipitation enhanced densities for the Empirical Canadian High Arctic Ionospheric Model (E-CHAIM)

Watson, C.; Themens, D. R.; Jayachandran, P. T.

DOI:  
[10.1029/2021SW002779](https://doi.org/10.1029/2021SW002779)

License:  
Creative Commons: Attribution (CC BY)

*Document Version*  
Publisher's PDF, also known as Version of record

*Citation for published version (Harvard):*  
Watson, C, Themens, DR & Jayachandran, PT 2021, 'Development and validation of precipitation enhanced densities for the Empirical Canadian High Arctic Ionospheric Model (E-CHAIM)', *Space Weather*, vol. 19, no. 10, e2021SW002779, pp. e2021SW002779. <https://doi.org/10.1029/2021SW002779>

[Link to publication on Research at Birmingham portal](#)

## General rights

Unless a licence is specified above, all rights (including copyright and moral rights) in this document are retained by the authors and/or the copyright holders. The express permission of the copyright holder must be obtained for any use of this material other than for purposes permitted by law.

- Users may freely distribute the URL that is used to identify this publication.
- Users may download and/or print one copy of the publication from the University of Birmingham research portal for the purpose of private study or non-commercial research.
- User may use extracts from the document in line with the concept of 'fair dealing' under the Copyright, Designs and Patents Act 1988 (?)
- Users may not further distribute the material nor use it for the purposes of commercial gain.

Where a licence is displayed above, please note the terms and conditions of the licence govern your use of this document.

When citing, please reference the published version.

## Take down policy

While the University of Birmingham exercises care and attention in making items available there are rare occasions when an item has been uploaded in error or has been deemed to be commercially or otherwise sensitive.

If you believe that this is the case for this document, please contact [UBIRA@lists.bham.ac.uk](mailto:UBIRA@lists.bham.ac.uk) providing details and we will remove access to the work immediately and investigate.



## RESEARCH ARTICLE

10.1029/2021SW002779

### Key Points:

- Satellite ultraviolet imager (UVI) measurements are used to develop a precipitation component for the Empirical Canadian High Arctic Ionospheric Model for high-latitude ionosphere density
- Comparisons with incoherent scatter radar measurements reveal significant improvement in density representation at 95–200 km altitude
- Precipitation enhanced densities are most sensitive to errors in satellite UVI data and selected electron energy spectrum

### Correspondence to:




C. Watson,  
[chris.watson@unb.ca](mailto:chris.watson@unb.ca)

### Citation:

Watson, C., Themens, D. R., & Jayachandran, P. T. (2021). Development and validation of precipitation enhanced densities for the Empirical Canadian High Arctic Ionospheric Model. *Space Weather*, 19, e2021SW002779. <https://doi.org/10.1029/2021SW002779>

Received 7 APR 2021  
Accepted 3 SEP 2021

# Development and Validation of Precipitation Enhanced Densities for the Empirical Canadian High Arctic Ionospheric Model

C. Watson<sup>1</sup> , D. R. Themens<sup>1,2</sup> , and P. T. Jayachandran<sup>1</sup> 

<sup>1</sup>Physics Department, University of New Brunswick, Fredericton, NB, Canada, <sup>2</sup>Space Environment and Radio Engineering (SERENE) Group, School of Engineering, University of Birmingham, Birmingham, UK

**Abstract** The Empirical Canadian High Arctic Ionospheric Model (E-CHAIM) provides the four-dimensional ionosphere electron density at northern high latitudes ( $>50^\circ$  geomagnetic latitude). Despite its emergence as the most reliable model for high-latitude ionosphere density, there remain significant deficiencies in E-CHAIM's representation of the lower ionosphere (below  $\sim 200$  km) due to a sparsity of reliable measurements at these altitudes, particularly during energetic particle precipitation events. To address this deficiency, we have developed a precipitation component for E-CHAIM to be driven by satellite-based far-ultraviolet (FUV) imager data. Satellite observations of FUV emissions may be used to infer the characteristics of energetic particle precipitation and subsequently calculate the precipitation-enhanced ionization rates and ionosphere densities. In order to demonstrate the improvement of E-CHAIM's ionosphere density representation with the addition of a precipitation component, this paper presents comparisons of E-CHAIM precipitation-enhanced densities with ionosphere density measurements of three auroral region incoherent scatter radars (ISRs) and one polar cap ISR. Calculations for 29,038 satellite imager and ISR conjunctions during the years 2005–2019 revealed that the root-mean-square difference between E-CHAIM and ISR measurements decreased by up to  $2.9 \times 10^{10}$   $\text{ele}/\text{m}^3$  (altitude dependent) after inclusion of the precipitation component at auroral sites, and by  $2.6 \times 10^9$   $\text{ele}/\text{m}^3$  in the polar cap. Improvements were most substantial in the winter season and during active auroral conditions. The sensitivity of precipitation-enhanced densities to uncertainties inherent to the calculation method was also examined, with the bulk of the errors due to uncertainties in FUV imager data and choice of distribution function for precipitation energy spectra.

**Plain Language Summary** The Empirical Canadian High Arctic Ionospheric Model (E-CHAIM) is a measurement-based model which provides the electron density of the upper atmosphere (the ionosphere) for a user-specified date, time, and location at northern high latitudes ( $>50^\circ$  geomagnetic latitude). The Earth's ionosphere can aid or disrupt the operation of technologies such as global navigation and radio communication systems, and thus ionosphere models are a critical component for reliable operation of these systems. E-CHAIM is currently the most reliable model for high-latitude ionosphere densities, which are particularly dynamic and complex due to the vertical orientation of Earth's high latitude magnetic field. A lack of reliable, widespread observations of the lower ionosphere (at roughly 95–200 km altitude) has resulted in deficiencies in E-CHAIM at these altitudes, mainly an inability to capture enhanced ionosphere densities associated with the precipitation of energetic particles that travel from near-Earth space, along Earth's magnetic field, and down into the atmosphere. To address this model deficiency, we have used satellite ultraviolet imager data as an indirect means of estimating enhanced ionosphere densities. Comparison of E-CHAIM densities with ground-based ionosphere density measurements has revealed that integration of these satellite-derived densities into E-CHAIM significantly improves model performance.

## 1. Introduction

The precipitation of energetic electrons and ions of magnetospheric and solar origin play a significant role in governing the structure and dynamic behavior of the high latitude ionosphere. Persistent particle precipitation in the auroral region, and to a lesser extent in the polar cap, is a significant source of neutral atmospheric ionization, which results in multi-scale ionosphere density structures that are complex in terms of

© 2021. The Authors.

This is an open access article under the terms of the [Creative Commons Attribution License](https://creativecommons.org/licenses/by/4.0/), which permits use, distribution and reproduction in any medium, provided the original work is properly cited.

morphology, evolution (temporal and spatial), and intensity. Because of this complexity, the development of models for high latitude ionosphere density has been a challenge. In addition, the development of empirical models has been hindered by the limited availability of reliable, direct, and widespread measurements of densities within the *D*, *E*, and lower *F* layers, particularly under precipitation conditions (Themens, Jayachandran, McCaffrey, Reid, & Varney, 2019). For example, ionosonde radars cannot provide electron density profiles during intense precipitation when *E*-region densities are larger than the *F*-region peak or when ionosonde transmissions are completely absorbed in the *D* and *E* layers. Additionally, inversions of satellite radio occultation measurements are impacted by cumulative downward propagation of errors which result in inaccurate lower ionosphere densities, particularly in regions with large horizontal density gradients (Yue et al., 2010).

Inaccurate high-latitude ionosphere models are problematic for radio propagation systems such as over-the-horizon-radar and long-range high-frequency radio communication, which depend on signal refraction in the ionosphere and thus accurate electron density representation for reliable operations (Jodalen et al., 2001; Zaalov et al., 2003). In addition, Global Navigation Satellite Systems (GNSS) require ionospheric correction for accurate positioning, and inaccurate ionosphere models can result in positioning errors of up to 100 m for single-frequency GNSS users (Hernández-Pajares et al., 2002). There are requirements for precision (centimeter-level) GNSS navigation in applications such as aviation, oil rig operation, agriculture, and automated mining and resource extraction (Perez-Ruiz & Upadhyaya, 2012; Sládková et al., 2011). With the widespread use of lower-cost single-frequency GNSS receivers and increasing infrastructure, resource exploration, and marine and aviation activity at high latitudes, access to accurate high latitude ionosphere densities is essential.

In recent years, the Empirical Canadian High Arctic Ionospheric Model (E-CHAIM) (Themens et al., 2017, 2018; Themens, Jayachandran, & McCaffrey, 2019) has emerged as the most reliable representation of electron densities at northern high latitudes ( $>50^\circ$  geomagnetic latitude; Maltseva & Nikitenko, 2020; Themens et al., 2020; Themens, Jayachandran, McCaffrey, Reid, & Varney, 2019). E-CHAIM is a significant improvement over other models such as the International Reference Ionosphere (IRI) at high latitudes, providing, for example, improvements of up to 60% in  $N_m F_2$  in the polar cap (Themens et al., 2017). Despite this improvement, E-CHAIM has limitations in its representation of the bottomside ionosphere, generally underestimating bottomside densities and performing poorly during energetic particle precipitation events (Themens, Jayachandran, & McCaffrey, 2019). This poor performance is due to the limited availability of reliable datasets for bottomside densities, as discussed above.

To address this limitation, we examine the feasibility of deriving precipitation enhanced profiles for E-CHAIM based on auroral far ultraviolet (FUV) emission observations of the Defense Meteorological Satellite Program (DMSP) Special Sensor Ultraviolet Spectrographic Imager (SSUSI; Paxton et al., 1992) and the Thermosphere Ionosphere Mesosphere Energetics and Dynamics (TIMED) Global Ultraviolet Imager (GUVI; Humm et al., 1998). SSUSI and GUVI measurements of atmospheric emission intensities at Lyman-Birge-Hopfield (LBH) wavelengths may be used to estimate electron energy flux and mean energy of precipitating electron populations (Germany et al., 1990; Lummerzheim et al., 1991; Sotirelis et al., 2013; Strickland et al., 1983, 1995). The energy flux and mean energy of precipitating electrons govern the atmospheric ionization rate and altitude of ionization, respectively, and are available as high-level GUVI and SSUSI data products. Given the high spatial resolution maps of GUVI and SSUSI data provided within a broad swath (thousands of kilometers) of the high-latitude region perpendicular to the spacecraft track, in addition to the multiple high latitude passes per day made by TIMED and DMSP satellites, the extensive historical GUVI and SSUSI datasets are a strong candidate to enhance E-CHAIM's performance in the presence of particle precipitation.

Derivation of precipitation-enhanced ionosphere densities from satellite ultraviolet imager (UVI) data has been previously examined by Aksnes et al. (2006), who added a precipitation component to IRI-95 ionosphere density profiles using UVI measurements of the Polar satellite. Atmospheric ionization rates were calculated from UVI-derived electron precipitation characteristics using the method introduced by Rees (1963). The authors found good agreement between precipitation-enhanced profiles and Tromsø incoherent scatter radar (ISR) measurements in the altitude range of 100–130 km during an interval of magnetospheric substorm activity on March 24, 1998. While the satellite UVI technique may only be used to

characterize precipitating electron populations up to  $\sim 20$  keV, Aksnes et al. (2006) also used Polar satellite X-ray emission measurements to characterize the precipitating electron population up to  $\sim 100$  keV, allowing for the calculation of enhanced *D*-region densities as well.

In this study, we present the development and validation of a “precipitation scheme” for E-CHAIM based on GUVI and SSUSI electron precipitation energy flux and mean energy data products. GUVI and SSUSI data are used to characterize precipitating electron populations with mean energies of 0–20 keV, and subsequently calculate precipitation-enhanced ionosphere densities for E-CHAIM. This energy range primarily impacts altitudes in the range of 100–200 km. In the precipitation scheme, atmospheric ionization rates due to electron precipitation are calculated using the Fang-2010 parameterization scheme (Fang et al., 2010), which provides monoenergetic ionization rates based on first-principle model results. Ionosphere densities are calculated from ionization rates under the assumption of a steady state ionosphere and using the current E-CHAIM as a background ionosphere, resulting in a final “precipitation-enhanced” E-CHAIM ionosphere density profile. ISR measurements at Poker Flat ISR (PFISR; 65.1°N, 212.5°E), Tromsø (69.5°N, 19.1°E), Sondrestrom (67.0°N, 309.1°E), and Resolute ISR north face (RISR-N; 74.7°N, 265.1°E) stations, which can provide electron density profiles ranging from *D*-layer altitudes and well into the topside *F*-layer depending on operation mode (Evans, 1969; Mathews, 1984), are used to validate precipitation-enhanced densities. A total of 29,038 profiles were compared with ISR measurements, corresponding to measurements taken during conjunctions of SSUSI/GUVI and ISR field-of-views for the years 2005–2019.

We have also examined the sensitivity of calculated precipitation-enhanced E-CHAIM profiles to uncertainties inherent to the precipitation scheme. The sensitivity analysis provides insight into whether deviations from ISR measurements may be attributed to uncertainties in the calculated precipitation-enhanced densities, and provides the relative error contributions of each precipitation scheme input. Sources of error inherent to the precipitation scheme include uncertainties in energy flux and mean energy values, choice of distribution function to represent the shape of the energy spectrum of precipitating electrons, uncertainties in neutral atmosphere composition and temperature values (required for the Fang-2010 parameterization), errors inherent to the Fang-2010 parameterization itself, and uncertainties in the atmospheric recombination rates required to calculate ionosphere density. Sensitivity analysis was conducted for all 29,038 SSUSI/GUVI-ISR conjunctions, by varying each input parameter within its respective uncertainty range and examining the subsequent variations in calculated precipitation-enhanced densities.

Section 2 describes the data sources and method used to calculate precipitation-enhanced densities for E-CHAIM. Section 3 presents comparisons of precipitation-enhanced densities with ISR measurements. Section 4 presents the sensitivity of calculated densities to uncertainties in precipitation scheme input parameters.

## 2. Data and Methodology

DSMP satellites have circular orbits at  $\sim 860$  km altitude with near-polar, sun-synchronous configurations. SSUSI data in this study are from four Block-5D3 DMSP satellites: F-16 (operational October 2003–August 2016), F-17 (operational November 2006–present), F-18 (operational October 2009–present), and F-19 (operational April 2014–February 2016). The TIMED satellite is in circular orbit at  $\sim 630$  km altitude and  $\sim 74^\circ$  inclination, with GUVI scan-mode data available for the period February 2002–December 2007.

SSUSI and GUVI instruments employ scanning imaging spectrographs to measure multispectral FUV auroral emission intensities (Humm et al., 1998; Paxton et al., 1992). Each instrument is equipped with a cross-track scanning mirror to adjust the field-of-view of the telescope and optical elements, allowing for horizon-to-horizon scans perpendicular to satellite motion and thus a spatially broad picture of FUV emission intensity rates along the spacecraft track. Atmospheric  $N_2$  emissions at LBH wavelength bands (140–152 nm 165–180 nm) respond to energetic particle precipitation, and measured emission rates at these wavelengths may be used to characterize the population of precipitating electrons (Germany et al., 1990; Sotirelis et al., 2013; Strickland et al., 1983, 1995). Based on precipitating particle energy deposition rates, calculated theoretically using transport models such as Boltzmann 3-Constituent (Strickland et al., 1976), LBH emission rates may be used to infer the energy flux ( $Q_0$ ) of precipitating electrons, while the average energy ( $E_0$ ; 0–20 keV) of the precipitating population can be derived from the ratio of short and long

**Table 1**  
*Incoherent Scatter Radar (ISR) Modes and Beam Configurations Used in This Study*

ISR	Orientation	Vertical bin size (km)	Time bin size (min)	Mode notes
Tromsø	Vertical	5	15	Predominantly Manda runs
Sondrestrom	<i>B</i> field-aligned	5	15	No mode preference selected
RISR-N	75° elev., 26° azi.	5	15	World Day runs—alternating code
PFISR	<i>B</i> field-aligned	5	15	Alternating code

*Note.* PFISR, Poker Flat ISR; RISR-N, Resolute ISR north face.

wavelength LBH emission rates. SSUSI  $E_0$  and  $Q_0$  data values are gridded in bin sizes of  $\sim 25 \times 25$  km, and are available as an “Auroral EDR” data product at <https://ssusi.jhuapl.edu/>. SSUSI data in this study are version 106, revision 0. GUVI  $E_0$  and  $Q_0$  data values are gridded in bin sizes of  $\sim 25 \times 25$  km, and are available as a Level 2B “EDR Aurora” data product at <http://guvitimed.jhuapl.edu/>. GUVI data used in this study are version 106, revision 1. As noted by Aksnes et al. (2006), UVI-derived  $Q_0$  may be unreliable when  $E_0 < 2$  keV due to the lack of  $O_2$  absorption of LBH emissions above  $\sim 150$  km.  $Q_0$  values have thus been set to zero in grid elements where  $E_0 < 2$  keV.

ISR electron density measurements are from the madrigal database (<http://isr.sri.com/madrigal/>). This study makes use of ISR data from the Tromsø, Sondrestrom, Poker Flat, and Resolute (north face only) systems. Data are processed in largely the same manner as Themens et al. (2018), where a probability distribution is created from 5 km vertical and 15-min temporal bins for each ISR and a log-normal distribution is fitted to estimate the appropriate electron density for each bin; however, compared to Themens et al. (2018), only a subset of configurations were used to better ensure the collocation of ISR profiles and GUVI/SSUSI pixel locations. ISR configurations are specified in Table 1.

At Resolute, there is a grating lobe near the radar vertical, so a beam off but close to vertical was selected instead of the vertical beam. The 75° elev., 26° azi. beam was chosen over the 85° elev., 26° azi. beam as the former has operated since initial deployment.

UVI-derived precipitation enhanced densities are compared with electron density measurements from four high-latitude ISRs, shown in Figure 1. Results are presented separately for auroral region and polar cap locations. ISR-SSUSI/GUVI conjunction events were considered when an ISR beam listed in Table 1 falls within one or more SSUSI/GUVI grid elements in the *E*-region or lower *F*-region (95–250 km), and when the time tags of SSUSI/GUVI and ISR measurements are within 7.5 min. For each such conjunction, SSUSI/GUVI data were averaged over grid elements intersected by the ISR beam at 95–250 km altitude. The number of SSUSI/GUVI grid elements involved in each conjunction varied between 1 and 4. A number of selection criteria for SSUSI/GUVI grid elements during ISR conjunctions were tested, which had negligible impact on results.

The Fang-2010 parameterization provides ionosphere ionization rates  $q_{\text{mono}}(E, h)$  at altitude  $h$  for electrons of energy  $E$ , and is based on solutions to Boltzmann transport equations, which describe where precipitating electrons deposit their energy in a neutral atmosphere. This parameterization has its heritage in a parameterization for auroral electron impact ionization proposed by Roble and Ridley (1987) and refined by Lummerzheim (1992). Inputs to the Fang-2010 scheme are electron precipitation energy, energy flux, and neutral atmospheric composition and temperature. In this study, altitude profiles of neutral atmosphere composition, density, and temperature data are from the empirical NRLMSISE-00 atmosphere model (Picone et al., 2002). The total population of precipitating electrons is specified based on SSUSI/GUVI  $E_0$  and  $Q_0$  data and the assumption of a particular distribution function to specify the shape of the energy spectrum for precipitating electrons. For model validation in this manuscript, we assume a Maxwellian distribution function. To investigate potential future improvements in implementation of the precipitation scheme, we also explore various spectral distribution functions for each ISR-UVI conjunction. Maxwellian, kappa, and Gaussian distributions are considered, which are the spectral shapes that best represent high latitude electron precipitation (Khazanov et al., 2014; Kletzing et al., 2003; Newell et al., 2009). Differential number flux  $dN/dE$  for each distribution function is as follows (e.g., McIntosh & Anderson, 2014):



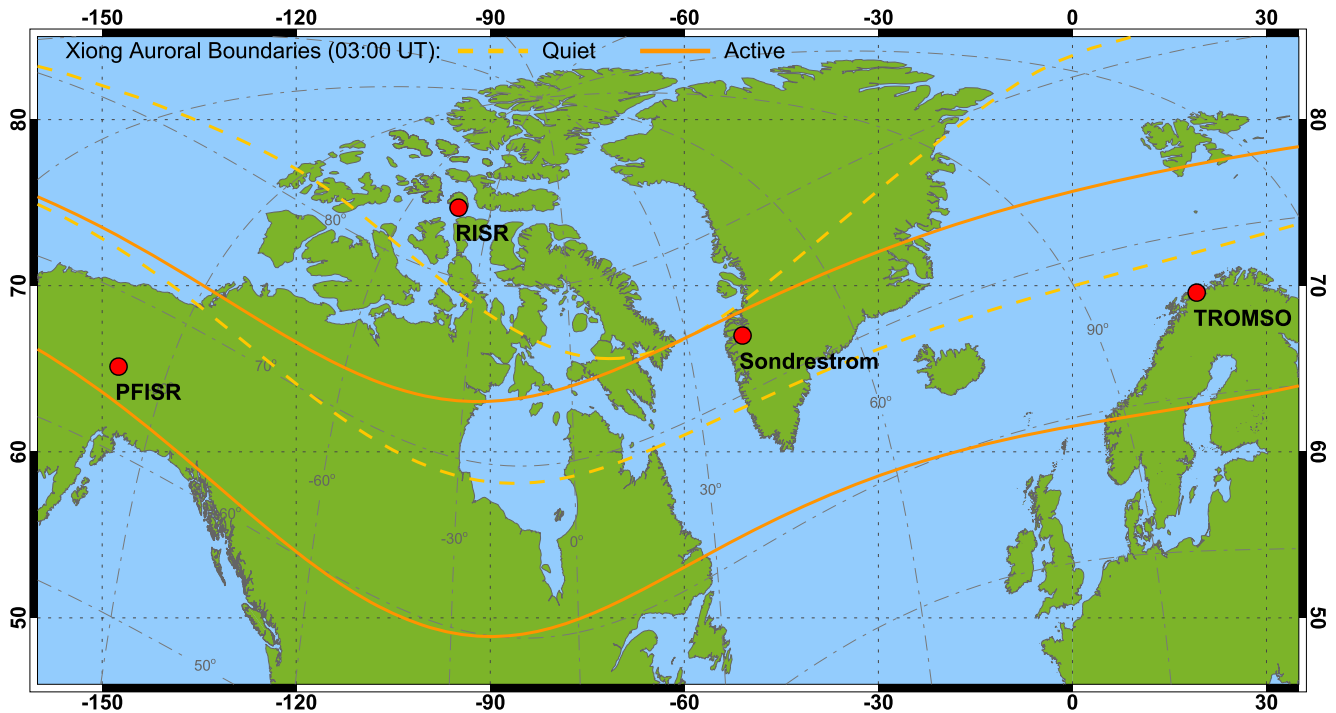


**Figure 1.** Map of incoherent scatter radar locations. Auroral boundaries of Xiong and Lühr (2014) are shown for quiet and active auroral periods at 03:00 UT.

$$\left(\frac{dN}{dE}\right)_{\text{Max}} = \frac{Q_0}{2E_0^3} E e^{-E/E_0} \quad (1)$$

$$\left(\frac{dN}{dE}\right)_{\text{Kap}} = \frac{(\kappa - 1)(\kappa - 2)}{\kappa^2} \frac{Q_0}{2E_0^3} \frac{E}{(1 + E / \kappa E_0)^{\kappa+1}} \quad (2)$$

$$\left(\frac{dN}{dE}\right)_{\text{Gau}} = \frac{Q_0}{\sqrt{2\pi}\sigma E_0} E e^{-\frac{(E-E_0)^2}{2\sigma^2}} \quad (3)$$

where  $\kappa$  is a dimensionless parameter that characterizes the shape of the high-energy tail of the kappa distribution ( $\kappa = 3$  is used in this work), and  $\sigma$  is the width of the Gaussian spectrum. Maxwell and kappa distributions are often used to characterize the electron precipitation associated with diffuse aurora, and are equivalent when  $\kappa \rightarrow \infty$ . Gaussian shapes are often associated with monoenergetic-type electron precipitation and discrete auroral arcs.

The total ionization rate ( $q_{\text{tot}}$ ) at height  $h$  is calculated by integrating monoenergetic ionization rates over all energies:

$$q_{\text{tot}}(h) = \int_{\text{all } E} q_{\text{mono}}(E, h) \frac{dN}{dE} E dE \quad (4)$$

A total of 3,000 logarithmically space energy bins are used in the integration, with bins progressively narrowing at lower altitudes. This total ionization rate can be related to the ionosphere electron density ( $N_e$ ) via the continuity equation:

$$\frac{dN_e}{dt} = q_{\text{tot}} + q_0 - \alpha N_e^2 + \bar{\nabla} \cdot (N_e \bar{v}) \quad (5)$$

where  $q_0$  is the background ionization rate,  $\alpha$  is the effective electron recombination rate in the ionosphere, and  $\bar{v}$  is the bulk ionosphere plasma velocity. We assume a steady state ionosphere and no significant plasma transport over our time scales of interest, thus the precipitation-enhanced ionosphere density is:

$$N_e(h) = \sqrt{\frac{q_{\text{tot}}(h)}{\alpha(h)} + N_{\text{E-CHAIM}}^2(h)} \quad (6)$$

where  $N_{\text{E-CHAIM}}$  is the background ionosphere density of E-CHAIM. Assumptions made in arriving at Equation 6 are discussed in Section 5. The additional ionization that results from the energy deposition of precipitating electrons combined with the “background” E-CHAIM densities produce a complete precipitation-enhanced electron density profile. This approach is similar in concept to that employed by Zhang et al. (2010) in their attempt to merge UVI-inferred NmE with that from the IRI. Effective recombination rates are from the empirical relationship of Gledhill (1986), which is based on 18 different data sources for electron density measurements and ionization rates. Given the limited data this relationship is based on, and the uncertainties associated with estimating ionization rates based on particle flux measurements of rockets and satellites, there is substantial uncertainty in the recombination rates, which is addressed in Section 4. Furthermore, this relationship is valid only between 50 and 150 km. In calculating precipitation-enhanced densities, we have included a smooth transition in the recombination rates above 150 km in order to suppress ionization at higher altitudes. Thus the precipitation scheme presented in this paper primarily modifies E-CHAIM densities below  $\sim 200$  km altitude.

Four examples of precipitation-enhanced densities (colored dashed lines) calculated for ISR-UVI conjunctions are shown in Figure 2, calculated for each spectral distribution function. Corresponding densities of non-precipitation E-CHAIM (dotted black lines) and ISR measurements (solid black lines) are also shown. Without the addition of the precipitation component, E-CHAIM underestimates densities below the *F*-region peak by up to three orders of magnitude, a common occurrence in the auroral region.

A total of 29,038 ISR-UVI conjunctions occurred from 2005 to 2019. Figure 3 shows the number of UVI observations binned according to  $E_0$  or  $Q_0$  (bins of 1 keV or 1 erg/cm<sup>2</sup>/s) and MLT (bins of 1 h) for auroral (a–f) and polar cap (g–l) ISRs, with number of observations in each bin indicated by color. Plots are organized horizontally according to auroral activity level, based on auroral electrojet (AE) indices taken from the OMNI database (<https://cdaweb.gsfc.nasa.gov/index.html/>).

Black dots are average  $E_0$  or  $Q_0$  for each 1 MLT bin. The bulk of SSUSI observations are from the morning and afternoon/evening due to the sun-synchronous DMSP orbits, and thus conjunctions are more concentrated in these MLT sectors. GUVI observations include all MLT sectors.  $E_0$  or  $Q_0$  for auroral region conjunctions generally increase away from local noon and with auroral activity level, where 49% of events for AE < 250 nT had no evident precipitation ( $Q_0 = 0.0$  erg/cm<sup>2</sup>/s), and 15% of events for AE > 500 nT had no evident precipitation. As expected, electron precipitation is less common and less intense at Resolute in the polar cap, and thus instances of enhanced *E*-region ionization are relatively infrequent. At Resolute,  $E_0$  and  $Q_0$  are generally larger during quiet auroral periods, with 65% of Resolute conjunctions during AE < 250 nT having no evident precipitation compared to 89% when AE > 500 nT. The use of a polar cap index as opposed to AE index at Resolute had negligible impact on results.

### 3. Comparison of Precipitation-Enhanced Profiles With ISR Measurements

For results presented in Figures 4–7, a Maxwellian energy distribution (Equation 1) is used to calculate precipitation enhanced densities. Alternative distribution functions are discussed later in this section and in Section 4. Figures 4 and 5 compare E-CHAIM and precipitation-enhanced densities with ISR measurements for altitudes of 90–300 km, for auroral and polar cap regions, respectively. First columns show average differences between ISR  $N_e$  and E-CHAIM  $N_e$  with the precipitation component in red, and without the precipitation component in black, where positive values indicate larger ISR  $N_e$ . Differences are averaged over all 29,038 events. Dotted profiles are average deviations above and below the means. The second columns in Figures 4 and 5 are root-mean-square (RMS) deviations between ISR and E-CHAIM  $N_e$ , and the third columns are the improvement in RMS deviations with the addition of the precipitation component. A negative improvement value indicates that E-CHAIM is more able to reproduce the ISR observations with the addition of the precipitation component. Plots are organized vertically according to AE index.

As shown in Figure 4, auroral region E-CHAIM densities without precipitation enhancement tend to underestimate those of ISR measurements below  $\sim 250$  km altitude. These differences increase with AE index,

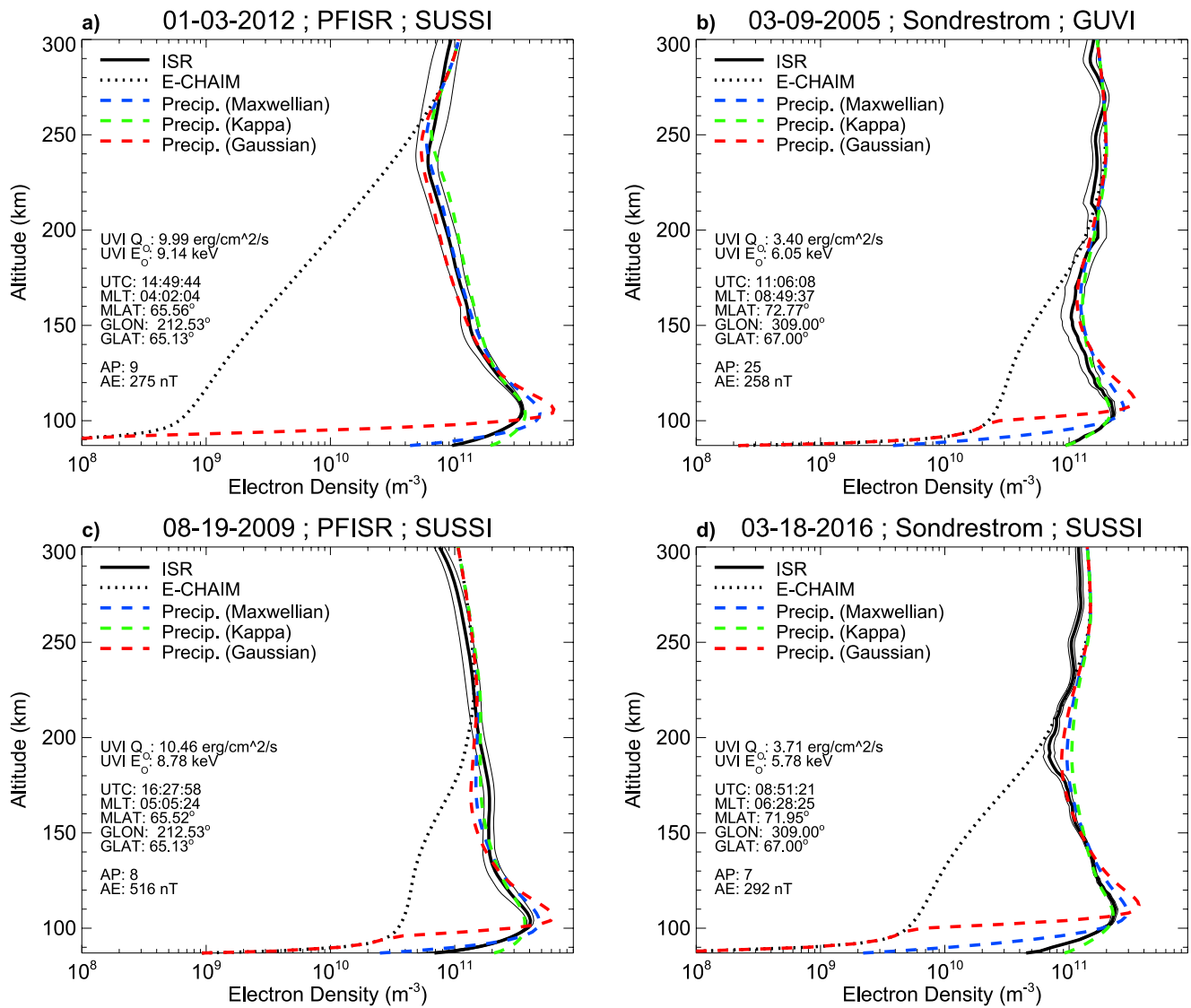


**Figure 2.** (a–d) Four examples of precipitation enhanced densities during incoherent scatter radar-ultraviolet imager (ISR-UVI) conjunctions, showing Empirical Canadian High Arctic Ionospheric Model (E-CHAIM) densities (dotted black lines), ISR densities (thick solid black lines) and uncertainties (thin solid black lines), and E-CHAIM densities with precipitation component (colored dashed lines) for three different energy spectrum distributions. GUVI, Global Ultraviolet Imager; PFISR, Poker Flat ISR; SSUSI, Special Sensor Ultraviolet Spectrographic Imager.

with an average difference of  $\sim 1.2 \times 10^{11}$  ele/m<sup>3</sup> at  $\sim 110$  km when AE > 500 nT (Figure 4g). Precipitation-enhanced densities eliminate the bulk of this systematic underestimation, with average differences from ISR measurements significantly closer to zero. Precipitation densities have a tendency to overshoot those of ISR measurements in some cases, particularly in the E-region when AE > 500 nT, with a  $\sim 2 \times 10^{10}$  ele/m<sup>3</sup> average overestimate at 100 km. RMS deviations in Figure 4 indicate a clear improvement in representation of ionosphere densities below  $\sim 200$  km with the precipitation scheme applied. Improvement is largest at  $\sim 110$ – $115$  km altitude and increases with AE index. Possible reasons for these observed trends are discussed in Section 5.

Improvements with the addition of the precipitation component are more modest in the polar cap (Resolute), as shown in Figure 5. Note, however, that E-CHAIM RMS deviations are significantly smaller compared with auroral RMS in Figure 4. Below 200 km altitude, differences between ISR measurements and models are  $< 4 \times 10^{10}$  ele/m<sup>3</sup>, on average, with a tendency for underestimation of ISR densities mainly in the



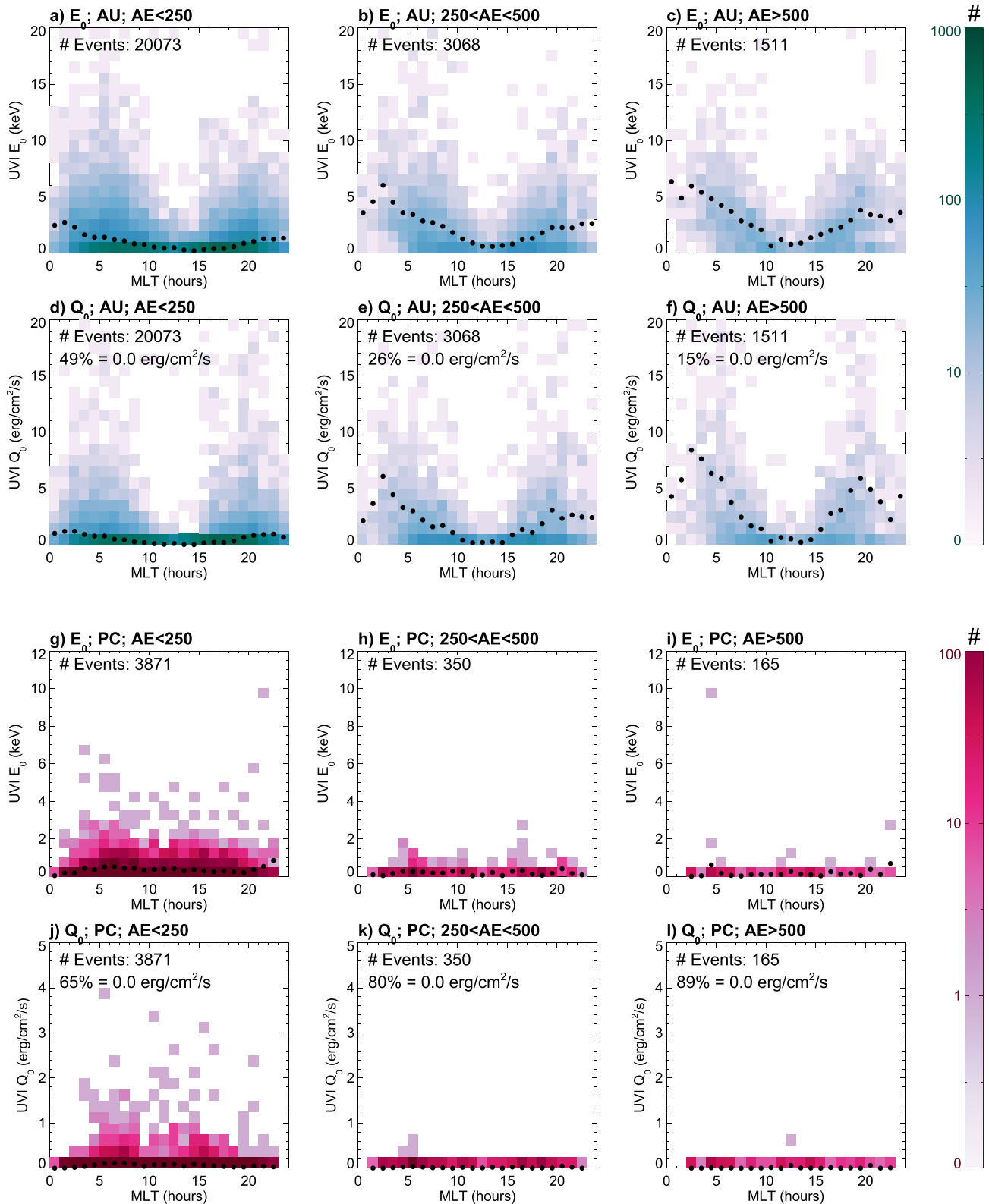


**Figure 3.** Two-dimensional histograms of satellite ultraviolet image (UVI)  $E_0$  and  $Q_0$  data for all incoherent scatter radar-UVI conjunctions. Green plots (a–f) are for auroral region stations, red plots (g–l) are for Resolute in the polar cap, and plots are organized horizontally according to auroral electrojet (AE) index. Black dots are binned average  $E_0$  or  $Q_0$ , in 1-h MLT bins.

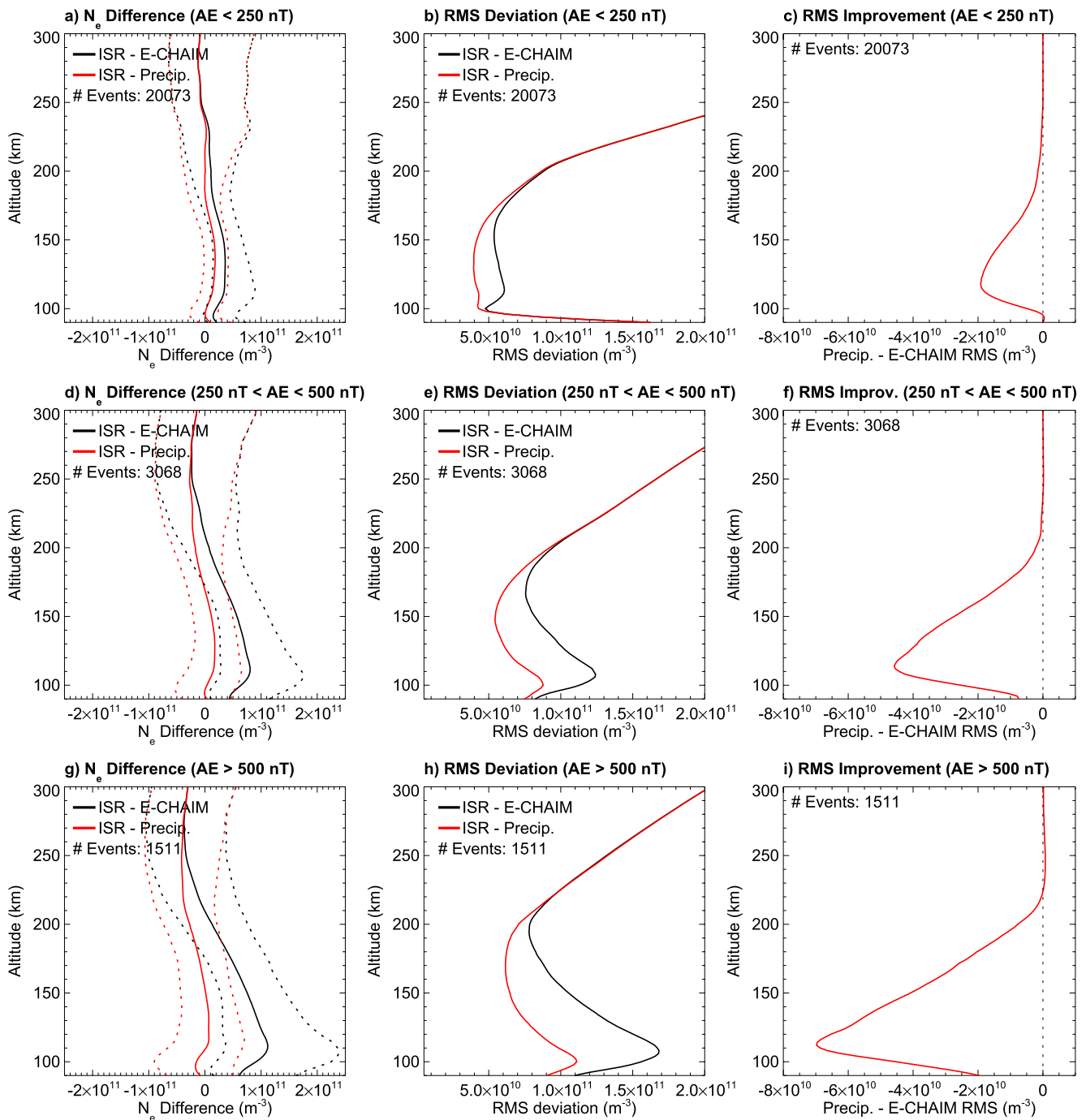


**Figure 4.** (a,d,g) Differences in auroral ionosphere densities of incoherent scatter radar (ISR) measurements and the Empirical Canadian High Arctic Ionospheric Model (E-CHAIM) with (red) and without (black) the precipitation component (left column), where positive indicates larger ISR values; (b,e,h) root-mean-square (RMS) deviations of E-CHAIM from ISR measurements (middle column); and (c,f,i) improvement of RMS deviations with the inclusion of a precipitation component in E-CHAIM (right column), where negative values indicate improved performance. Plots are organized vertically according to auroral electrojet (AE) index.

lower  $F$ -region. The bulk of the improvement from precipitation enhanced densities arises during low AE intervals between 105 and 180 km (Figure 5c), with negligible improvement during higher AE intervals.

For all ISR-UVI auroral region conjunctions, Figures 6 and 7 show normalized histograms of the differences between  $\log_{10}(\text{ISR } N_e)$  and  $\log_{10}(\text{E-CHAIM } N_e)$  at 110 km altitude for 06:00–18:00 MLT (dayside) and 18:00–

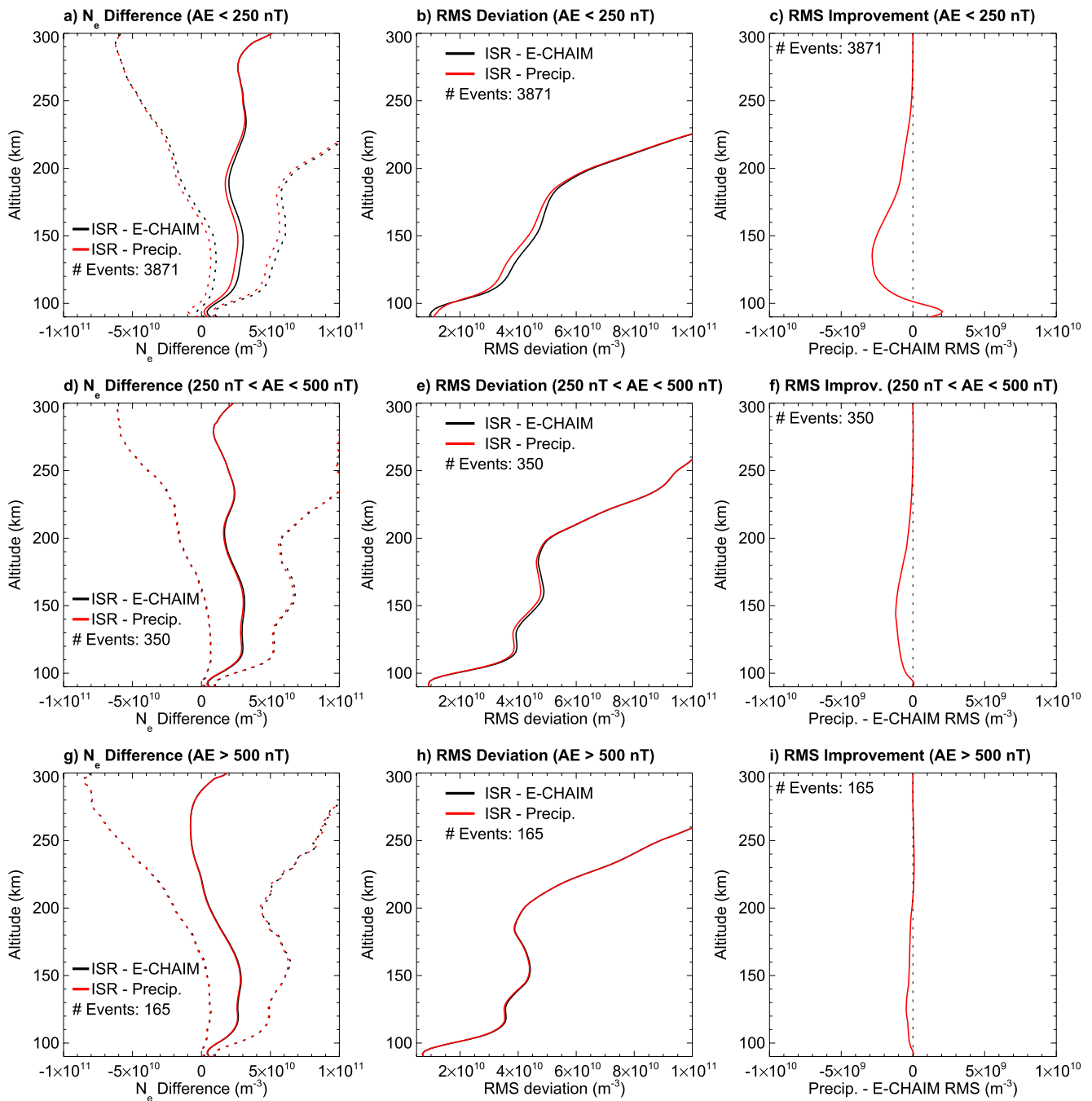
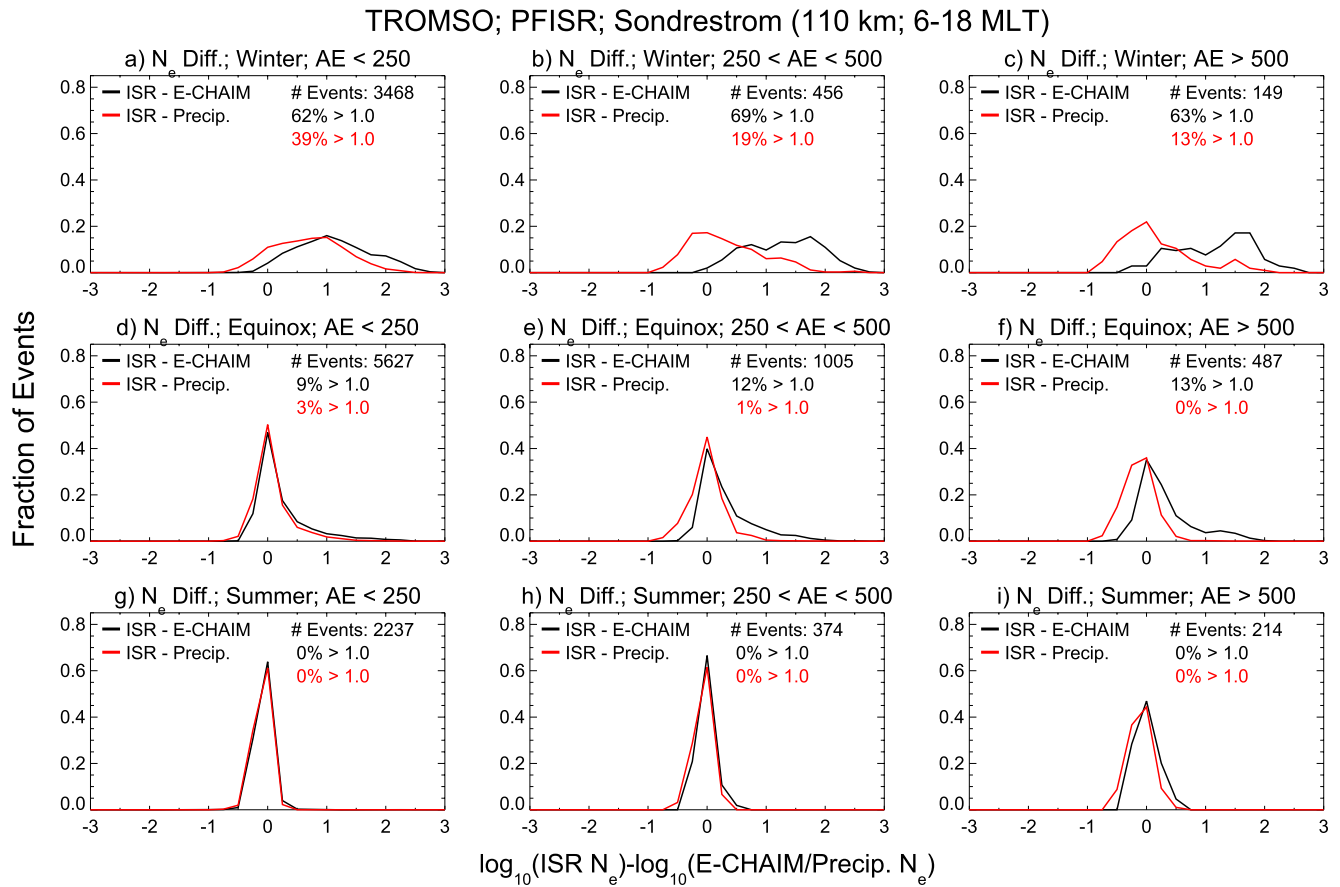


Figure 5. Same as Figure 4, but for the polar cap region.

06:00 MLT (nightside) sectors, respectively. Histograms in red are with the inclusion of the precipitation component, and histograms in black are without. Plots in each figure are organized horizontally according to AE index and vertically according to season. Logarithms of densities are used here to highlight the order-of-magnitude (OOM) deviations from ISR measurements. The fraction of conjunctions with larger than one OOM difference in ISR and model densities are indicated in each panel. OOM differences at Resolute are not significant and have been omitted.

In Figures 6 and 7, OOM deviations from ISR measurements are largest and most common during the winter seasons, in the night sector, and increase with AE index. Without the precipitation component,



**Figure 6.** Auroral region normalized histograms of  $\log_{10}(\text{ISR } N_e)$  minus  $\log_{10}(\text{E-CHAIM } N_e)$  with (red) and without (black) the inclusion of the precipitation component, at 110 km altitude for the 06:00–18:00 MLT sector. Plots are organized vertically according to (a–c) winter, (d–f) equinox, and (g–i) summer seasons, and horizontally according to auroral electrojet (AE) index. E-CHAIM, Empirical Canadian High Arctic Ionospheric Model; ISR, incoherent scatter radar.

E-CHAIM underestimates ISR measurements at 110 km by more than 1 OOM more than 60% of the time during daytime winter (Figures 6a–6c) and more than 90% of the time during nighttime winter (Figures 7a–7c). The most significant improvements during winter with addition of the precipitation component are during high AE intervals, with only 13% of events during daytime and 9% of events during nighttime resulting in differences larger than 1 OOM when  $\text{AE} > 500$  nT.

During  $\text{AE} < 250$  nT intervals in winter, a significant portion of E-region enhancements are not accounted for by SSUSI/GUVI observations, with a small leftward shift in the red distribution shown in Figure 6a, and a bi-modal type distribution shown in red in Figure 7a. These events involve enhancements in the lower ionosphere observed in ISR measurements, but little to no LBH emissions observed by SSUSI or GUVI. During equinox, E-CHAIM underestimates of E-region density are less common during daytime when less than 15% of events have OOM differences, and more common during night when more than 50% of events have OOM differences. The precipitation scheme provides improvement in most of these events, resulting in less than 3% with OOM differences during day, and less than 19% (6%) during night when  $\text{AE} < 250$  nT ( $> 500$  nT). There are no OOM differences between E-CHAIM and ISR measurements during summer daytime (Figures 6g–6i), and few ( $< 7\%$ ) OOM E-CHAIM underestimates of ISR measurements during summer nighttime (Figures 7g–7i), which are all accounted for by GUVI/SSUSI observations. In the Summer months, solar EUV is the dominant ionization mechanism at high latitudes, and ionization due to energetic particle precipitation may play a lesser role. Possible implications of these observations are discussed in Section 5.

We have also tested the accuracy of UVI-based precipitation enhanced densities by taking best-fits of all ISR measurements to infer the ideal input  $E_0$  and  $Q_0$ , and comparing with SSUSI/GUVI measurements. “Ideal”

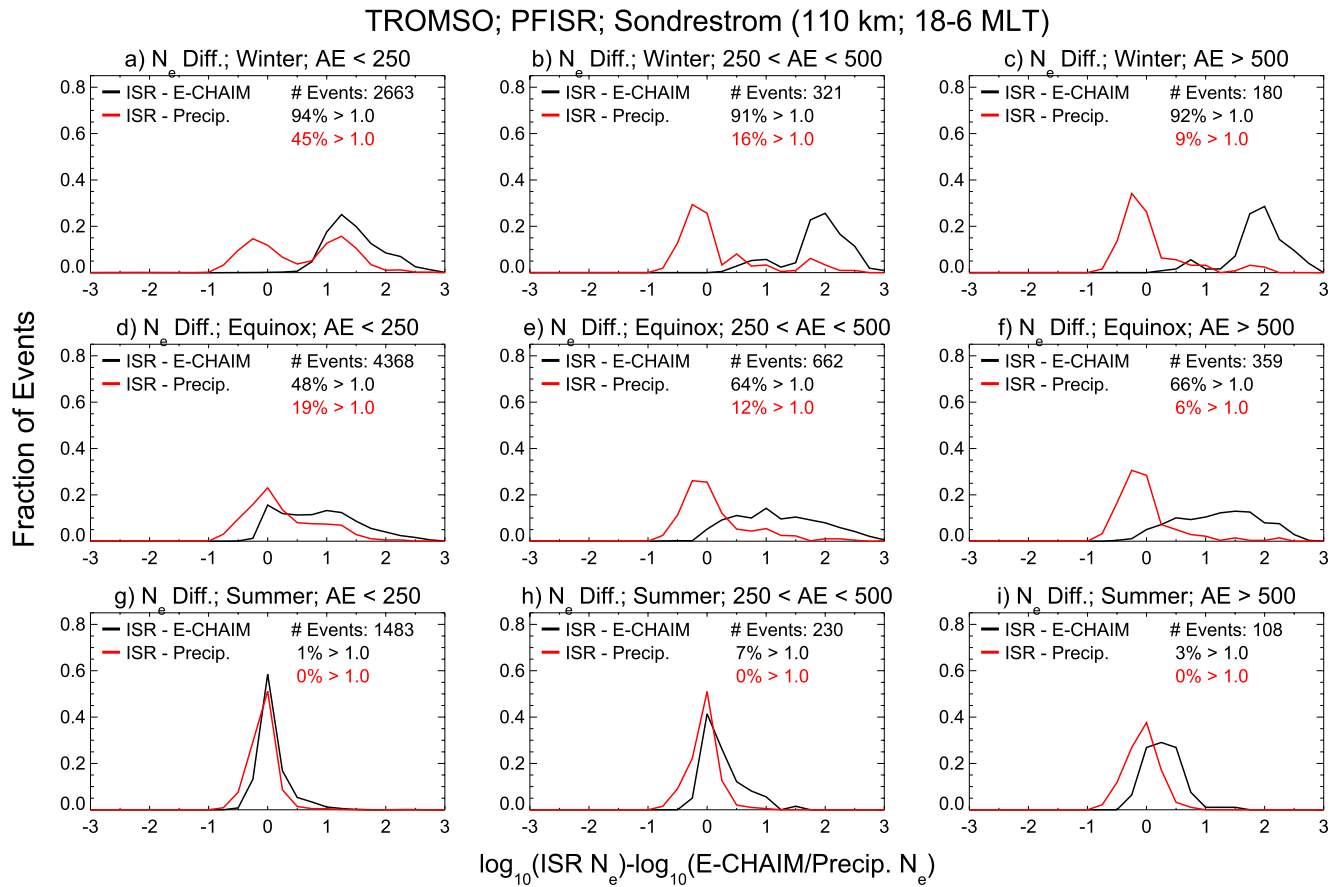


**Figure 7.** Same as Figure 6, but for the 18:00–06:00 MLT sector.

input  $E_0$  and  $Q_0$  refer to the inputs to the precipitation scheme that best reproduce ISR observations. This procedure involves iterations through input  $E_0$  values of 0.0–20.0 keV and  $Q_0$  values of 0.0–100.0 erg/cm<sup>2</sup>/s. E-CHAIM is used as the background ionosphere density, as in Equation 6. A precipitation enhanced density is calculated for each iteration, along with a least-squares-fit to ISR densities at altitudes of 95–140 km. The ideal input  $E_0$  and  $Q_0$  are based on the iteration that results in the best fit to ISR measurements.

Figure 8 shows results of this procedure, for all ISR-GUVI/SUSSI conjunctions. Results are shown in the form of two-dimensional histograms, where vertical axes are differences between ideal input parameters and corresponding UVI  $E_0$  and  $Q_0$ , and horizontal axes are MLT. Bin sizes for histograms are 1 h MLT and 1 keV or 1 erg/cm<sup>2</sup>/s. Color indicates number of events in each bin. Figures 8a–8f are for auroral region events and Figures 8g–8l are for Resolute conjunctions in the polar cap. Plots are organized horizontally according to AE index.

The bulk of conjunctions at all sites show  $E_0$  and  $Q_0$  differences concentrated within  $\pm 5$  keV and  $\pm 5$  erg/cm<sup>2</sup>/s, with a larger portion of auroral region UVI data deviating from ideal ISR values during high AE intervals (Figures 8c and 8f). It is noted that low energy and flux events are more common during low AE intervals (see Figure 3), and that deviations from ideal ISR  $E_0$  and  $Q_0$  tend to be larger for higher energy and flux events. Thus larger differences are expected during high AE intervals. In the morning sector in the auroral region, there are a significant number of events where UVI  $E_0$  is less than ideal, particularly during quiet auroral periods (Figure 8a). These events are in large part associated with the OOM winter underestimates of ISR densities by the precipitation scheme during quiet times in Figures 6a and 7a. A smaller number of events resulted in larger than ideal UVI  $E_0$  values in the morning sector, while UVI  $E_0$  data in the afternoon/evening sector was generally closer to ideal for all auroral activity levels. The UVI  $Q_0$  data generally performed quite well in the auroral region (Figures 8d–8f) compared with the UVI  $E_0$  data,



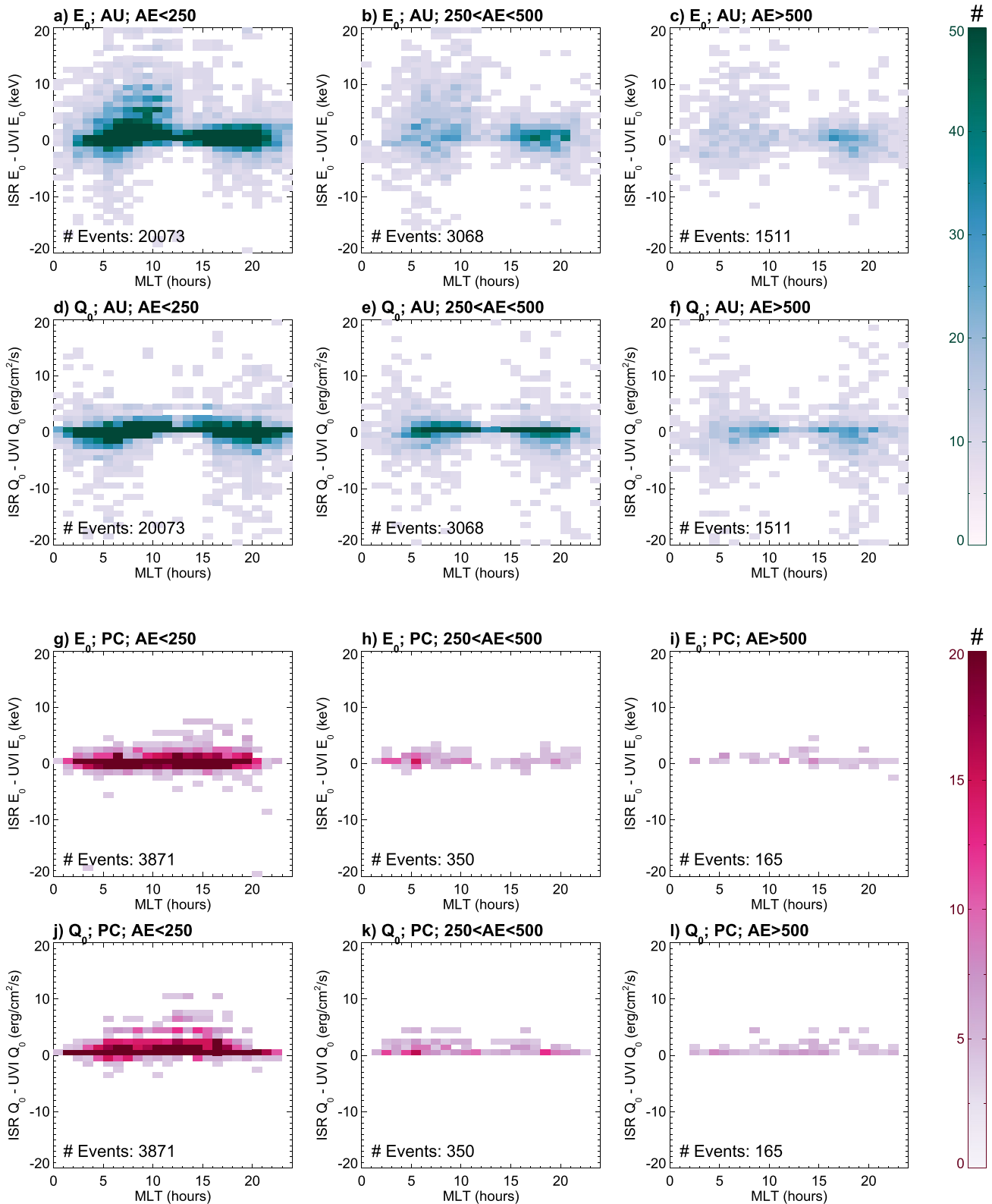


**Figure 8.** For auroral (a–f) and polar cap (g–i) regions, two-dimensional histograms of ideal  $E_0$  and  $Q_0$  values derived from incoherent scatter radar (ISR) best fits, minus corresponding satellite ultraviolet image (UVI)  $E_0$  and  $Q_0$ , binned according to MLT. Plots are organized horizontally according to auroral electrojet (AE) index.

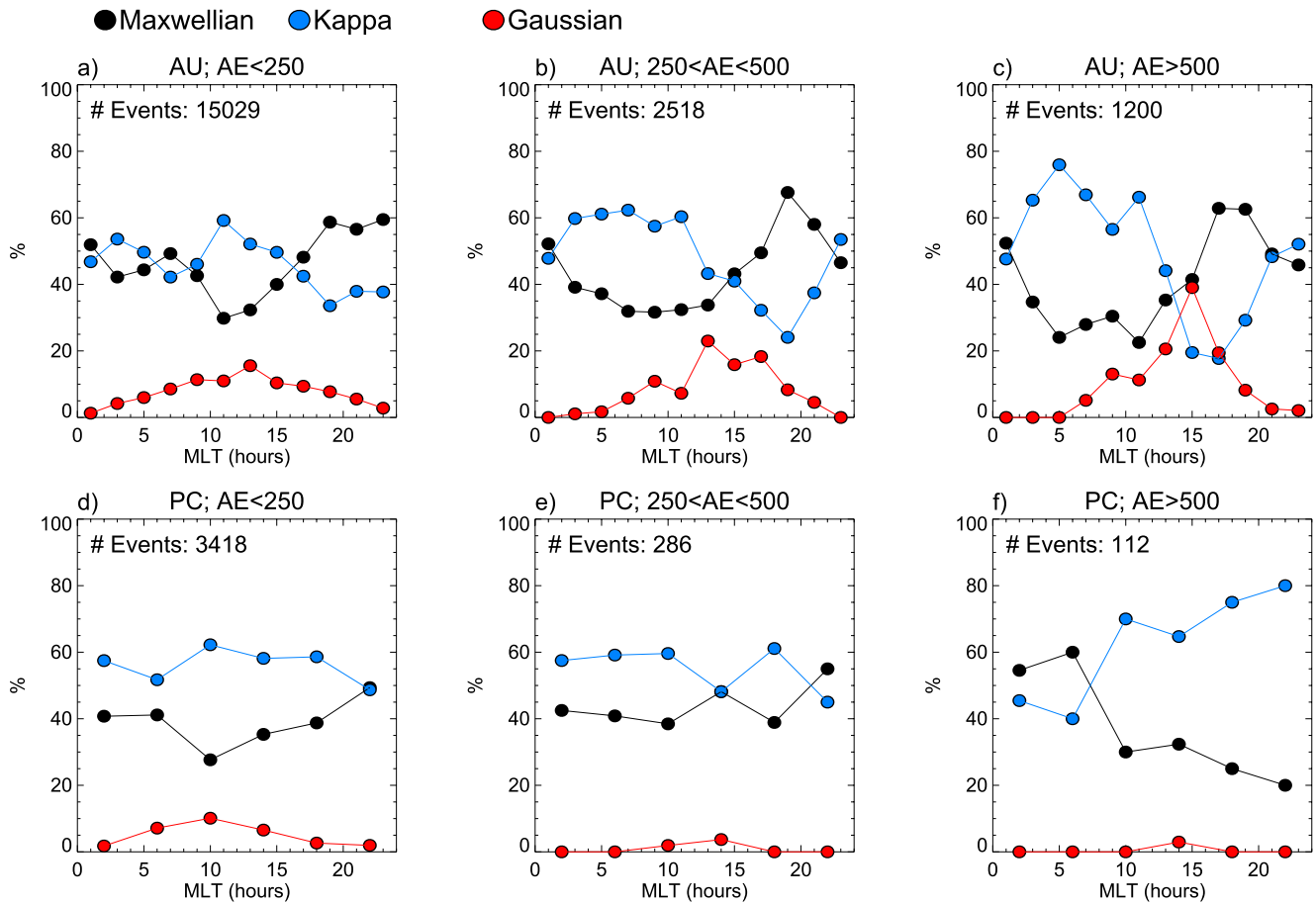


**Figure 9.** For auroral (a–c) and polar cap (d–f) regions, the percentage of events that resulted in incoherent scatter radar (ISR) best fits for each test energy spectrum shape. AE, auroral electrojet.

with a tendency for UVI  $Q_0$  to overshoot the ideal ISR values in both the morning and afternoon/evening sectors. Notably in the polar cap, there is a tendency for UVI  $Q_0$  values to be less than ideal (Figures 8j–8l), consistent with the underestimation of ISR densities in the lower ionosphere shown in Figure 5 by both E-CHAIR and the precipitation enhanced densities.

For potential future improvements in implementation of the precipitation scheme, we also explore ideal spectral distribution functions to apply in Equation 4. Again we refer to an “ideal” spectral distribution as the one which results in the best fit to ISR measurements. For all ISR-UVI conjunctions, we again iterate through  $E_0$  and  $Q_0$  as described above, but also add an iteration through Maxwellian, Kappa, and Gaussian distribution functions (Equations 1–3). The ideal spectral distributions is based on the iteration that results in the best fit to ISR measurements. Figure 9 shows the ideal energy spectra according to ISR best fits. Note that results shown only include events with nonzero ideal  $E_0$  and  $Q_0$  values. Results for auroral (a–c) and polar cap (d–f) events are organized horizontally according to AE index, with the percentage of events corresponding to each spectral shape plotted in bins of 2 MLT for auroral events and 4 MLT for polar cap events. A Maxwellian or kappa distribution is ideal in most cases in both polar cap and auroral regions. In the auroral region, the Kappa distribution is more often ideal in the morning and early afternoon sector, while the Maxwellian is the preferred spectral shape in the late afternoon and evening sectors. These local time trends become more pronounced as auroral activity increases. Cases where a Gaussian distribution is ideal also increases with auroral activity, where up to 40% of events in the 14:00–16:00 MLT sector are best characterized by a Gaussian distribution when AE > 500 nT (Figure 9c). Newell et al. (2009) showed an increase in the occurrence of monoenergetic-type aurora in the afternoon sector during high solar wind-magnetosphere coupling intervals, based on DMSP SSJ particle data. This increase in discrete auroral occurrence

may contribute to the increased occurrence of Gaussian best fits in this sector. Kappa distributions are most often ideal in the polar cap, particularly during active auroral periods, with the exception of the early morning sector (Figure 9f). Gaussian distributions are less often ideal in the polar cap, with up to 10% occurrence of such cases in the dayside when  $AE < 250$  nT (Figure 9d).

#### 4. Error Analysis

There are a number of sources of error associated with the calculation of precipitation-enhanced densities. This analysis addresses whether errors inherent to the precipitation scheme may account for differences between ISR measurements and precipitation-enhanced densities. We also examine the sensitivity of precipitation-enhanced densities to uncertainties of each input parameter of the precipitation scheme, which may be used to improve the implementation of the precipitation scheme in E-CHAIM in the future.

Derivation of GUVI and SSUSI  $E_0$  and  $Q_0$  data involve a number of steps including instrument calibration, subtraction of dayglow emissions, removal of MeV noise, and subtraction of precipitating proton contributions (Germany et al., 1990; Paxton et al., 1992; Strickland et al., 1995). Based on these calibration and modeling steps, Germany et al. (1997) estimated a 72% 1-sigma uncertainty level in UVI  $E_0$  and  $Q_0$  data. We use this 72% uncertainty level in our error analysis. For comparison to the Germany et al. uncertainty, we have also carried out comparisons of SSUSI  $E_0$  and  $Q_0$  data with corresponding values derived from DMSP Special Sensor J (SSJ) particle data (Redmon et al., 2017), which provides precipitating electron flux in 20 energy bands between 30 eV and 30 keV. Comparisons were done for all ISR-UVI conjunctions where the spacecraft magnetically mapped to within 100 km of the respective ISR station, and where SSJ data were available. Based on these comparisons we found 1-sigma uncertainty levels of 68% for UVI  $E_0$  values and 79% for UVI  $Q_0$ , where discrepancies between SSJ and UVI values increased with energy and flux. These comparisons roughly agree with the uncertainty levels of Germany et al. (1997), although  $E_0$  and  $Q_0$  values derived from SSJ data also inherit some uncertainty due to the 30 keV upper limit in observable energy.

Mass density and neutral temperatures of the NRLMSISE-00 model are used as inputs to the Fang-2010 parameterization for atmospheric ionization rates. Based on extensive model comparisons with measurements of the neutral atmosphere, Picone et al. (2002) found uncertainty ranges of  $-8.35\%$ – $16.21\%$  and  $-30.85$ – $1.48$  K for NRLMSISE-00 density and temperature, respectively. Fang et al. (2010) indicated that monoenergetic ionization rates of the Fang-2010 parameterization scheme contained 5% uncertainty, at most, based on comparisons with model runs. Although some of this maximum 5% may be attributed to atmosphere inputs, we test the sensitivity of precipitation-enhanced profiles to NRLMSISE-00 uncertainties and the 5% Fang-2010 uncertainty separately.

Sensitivity of UVI-derived densities to uncertainty in effective recombination rates is estimated by testing the recombination rates of various sources. In addition to the Gledhill (1986) rates, we also test the empirical relationship of Vickrey et al. (1982), which is based on ISR and rocket sounding data, and the electron temperature dependent expressions for dissociative recombination rates of Schunk and Nagy (2009) and Sheehan and St. Maurice (2004), which are based on previous laboratory measurements of  $N_2^+$ ,  $O_2^+$ , and  $NO^+$  recombination rates. We obtain ionosphere electron temperatures from the IRI-2016 (Bilitza et al., 2017).

The choice of distribution function to construct precipitating electron populations also impacts final precipitation-enhanced density profiles. A Maxwellian function (Equation 1) was used for results presented in Section 4. The sensitivity of calculated densities to choice of distribution function is evaluated by applying Kappa and Gaussian distributions (Equations 2 and 3) to the precipitation scheme, and comparing with densities calculated using the Maxwellian distribution.

Table 2 summarizes the input parameters to the precipitation scheme and associated uncertainties.

The sensitivity of the precipitation scheme to uncertainties in input parameters has been tested for all ISR-UVI conjunctions. Figure 10 shows the average variability in precipitation enhanced densities associated with the uncertainty range of each input parameter (color coded), or associated with the various choices of input option in the case of recombination rates and energy spectrum shape. The cumulative uncertainty range (maximum possible variability in calculated density) is shown in black. Uncertainties are shown at 8 different altitudes (centered on the total uncertainty ranges in black), and for four different  $Q_0$  ranges based

**Table 2**  
*Uncertainties/Range of Values of Parameters for Calculating Precipitation Enhanced Densities*

Input parameter	Uncertainty/range of values
GUVI/SSUSI $Q_0$	$\pm 75\%$
GUVI/SSUSI $E_0$	$\pm 75\%$
NRLMSISE-00 mass density	$-8.35\%$ – $16.21\%$
NRLMSISE-00 temperature	$-30.85$ – $1.48$ K
Fang-2010 ionization rates	$\pm 5\%$
Recombination rates	Gledhill (1986), Vickrey et al. (1982), Sheehan and St. Maurice (2004), Schunk and Nagy (2009)
Distribution function	Maxwellian, Kappa, Gaussian (Equations 1–3)

*Note.* GUVI, Global Ultraviolet Imager; SSUSI, Special Sensor Ultraviolet Spectrographic Imager.

on the SSUSI/GUVI  $Q_0$  data. Dashed gray line contours indicate the percentage of ISR density-precipitation-enhanced density differences that fall within each respective contour pair. For example, the two 98% contours in each panel enclose the range of density differences observed in 98% of the ISR-UVI conjunctions. So at 120 km altitude in Figure 10a, 98% of the time the difference between ISR and precipitation-enhanced densities is between  $-1.0e11$   $m^{-3}$  and  $1.1e11$   $m^{-3}$ . These contours are included as a guide to indicate the percentage of density differences that fall within the total uncertainty ranges. Positive  $\Delta N_e$  values indicate an increase in the precipitation enhanced density when a particular input parameter is varied, as well as an underestimate of ISR measurements by precipitation enhanced densities in the case of gray contours.

Sensitivity of precipitation enhanced densities to variations in input parameters generally increases with SSUSI/GUVI  $Q_0$ , given that the contribution of the precipitation component to the overall density will be larger when there is more precipitating particle flux. For lowest flux events in Figure 10a, sensitivity to each input parameter is relatively small, with variations in UVI  $Q_0$  and  $E_0$  data having the largest contribution depending on altitude. Total uncertainty ranges are within  $\pm 1e11$   $m^{-3}$ , which is relatively small compared to larger flux situations, but still a large uncertainty range for ionosphere density. Seventy-five percent of the ISR-UVI-derived density differences fall within the total uncertainty bounds at most altitudes, indicating that uncertainties of the precipitation scheme in Table 1 can account for the bulk of the differences observed in ISR measurements and UVI-derived densities in Figures 4–7. An exception is at higher altitudes  $>200$  km, where the precipitation scheme uncertainty accounts for  $<50\%$  of observed density differences, and where errors in the E-CHAIM model itself are likely more dominant.

In higher flux situations (Figures 10b–10d), precipitation enhanced densities are most sensitive to variations in  $Q_0$ ,  $E_0$ , and choice of energy distribution function, with smaller increases in the uncertainty contributions of other inputs. Largest uncertainties due to recombination rates, atmosphere mass density, atmosphere temperature and the Fang-2010 ionization rates are  $\sim 7e10$   $m^{-3}$  at 115 km,  $\sim 4e10$   $m^{-3}$  at 100 km,  $\sim 9e10$   $m^{-3}$  at 100 km, and  $\sim 1e10$   $m^{-3}$  at 100 km, respectively, when  $Q_0 > 10$  erg/cm<sup>2</sup>/s. UVI  $E_0$  is the dominant uncertainty source at higher altitudes  $>130$  km, with a primarily positive uncertainty range of up to  $2.5e11$   $m^{-3}$  for  $Q_0 > 10$  erg/cm<sup>2</sup>/s events. Uncertainty due to UVI  $E_0$  is primarily negative at E-region altitudes, up to  $-4e11$   $m^{-3}$ . Uncertainties in UVI  $Q_0$  becomes increasingly important toward lower F and E-region altitudes, as large as  $\pm 2.5e11$   $m^{-3}$  at 100 km, and choice of spectral shape is most impactful on E-region densities, with uncertainties as large as  $\pm 2.5e11$   $m^{-3}$ . Total uncertainty in precipitation enhanced densities is as large as  $\pm 6.0e11$   $m^{-3}$  at E-region altitudes when  $Q_0 > 10$  erg/cm<sup>2</sup>/s. For the most part, 75% and often 90% contours fall within the total uncertainty levels in Figures 10b–10d, again with the exception of higher altitudes  $>200$  km.

Figure 11 shows the average variability of precipitation enhanced densities, but as a percentage of the initial precipitation-enhanced density (before any input parameter modification). These are plotted in a single panel since, as density increases with input precipitation flux, the percent variability remains largely consistent for all  $Q_0$  levels. Again, Figure 11, shows the dominant sources of error to be UVI  $Q_0$  and  $E_0$  at most altitudes, with choice of energy spectrum increasingly important at lower altitudes. Total average

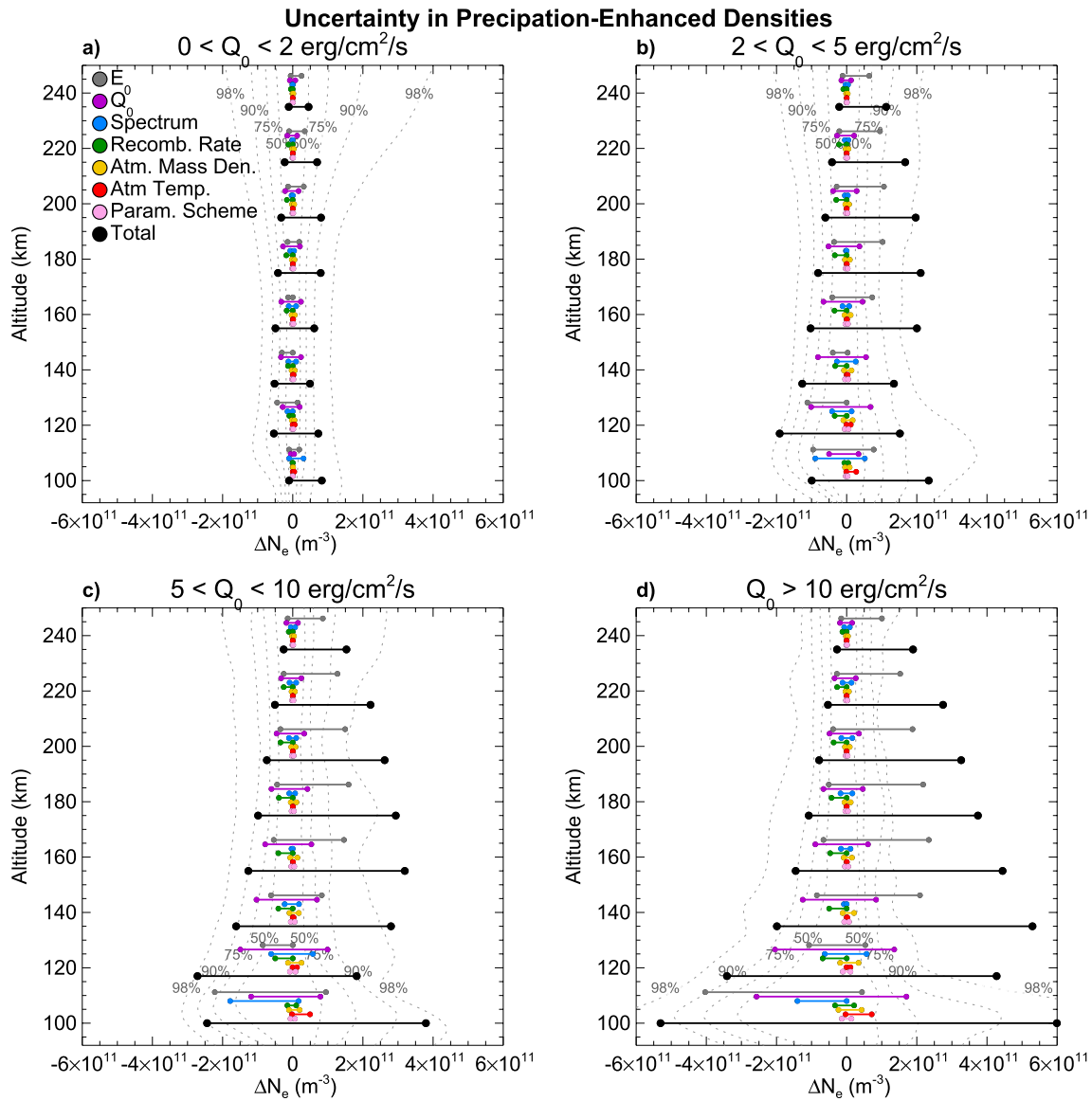


**Figure 10.** (a–d) Sensitivity of precipitation enhanced densities to uncertainties associated with each input parameter (color coded), along with total uncertainty in final precipitation enhanced densities (in black). Sensitivity ranges at each altitude are averaged over all incoherent scatter radar-ultraviolet image (ISR-UVI) conjunctions. Sensitivities are plotted separately for four different ranges of UVI  $Q_0$ . Dashed gray contours represent the percentage of conjunctions resulting in respective ISR-modeled density differences, as described in the main text body.

uncertainties were largest at 180–200 km, in the range of  $\pm 100\%$ , with the exception of *E*-region altitudes where average uncertainties approached  $-136\%$ .

Figure 12 presents sensitivity of peak *E*-region density ( $NmE$ ) and altitude of peak density ( $hmE$ ) of precipitation enhanced profiles to variations in precipitation scheme parameters. A comparison between ISR  $NmE$  and  $hmE$  values and those derived from the precipitation scheme showed no significant correlation (Figure 13), which is not surprising given the uncertainty levels involved. Dashed gray lines show contours below which the respective percentages of  $NmE$  or  $hmE$  differences (ISR minus precipitation scheme) fall.

Figure 12a shows the  $NmE$  uncertainties as a function of SSUSI/GUVI  $Q_0$  (the dominant factor in  $NmE$  determination) for each input parameter as well as the cumulative uncertainty. Dots are results of individual ISR-UVI conjunctions and lines are power law best fits. The corresponding power laws are listed in the figure.  $NmE$  uncertainties are relatively predictable for all input parameters, increasing with UVI  $Q_0$  according



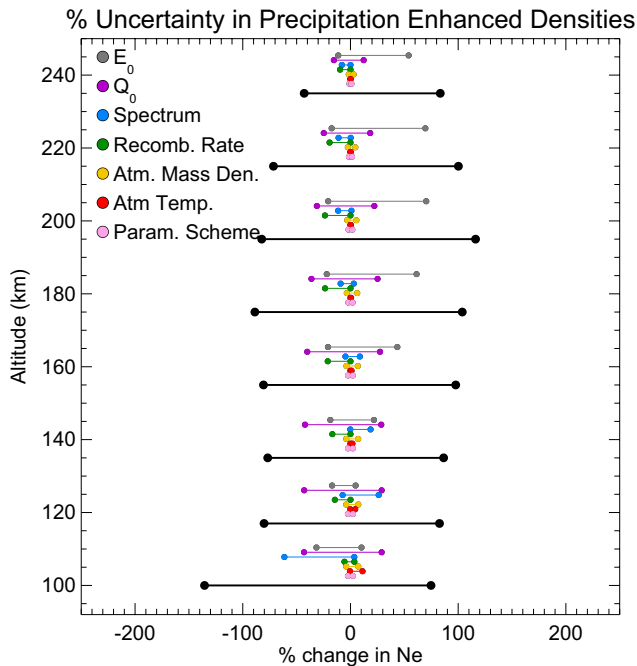


**Figure 11.** Sensitivity of precipitation enhanced densities (in percent change in  $N_e$ ) to uncertainties associated with each input parameter (color coded), along with total uncertainty in final precipitation enhanced densities (in black). Sensitivity ranges at each altitude are averaged over all incoherent scatter radar-ultraviolet image conjunctions.

to the corresponding power law. Uncertainties in  $Q_0$  and spectral shape are the largest factors in NmE uncertainties, approaching  $7e11 \text{ m}^{-3}$  and  $4.5e11 \text{ m}^{-3}$  at UVI  $Q_0 = 30 \text{ erg/cm}^2/\text{s}$ , respectively. Note that the bulk of events involve UVI  $Q_0$  values less than  $10 \text{ erg/cm}^2/\text{s}$ , corresponding to cumulative NmE uncertainties of up to  $\sim 8e11 \text{ m}^{-3}$ , however more extreme UVI  $Q_0$  events result in NmE uncertainties surpassing  $1.5e12 \text{ m}^{-3}$ . The bulk of cumulative percent NmE uncertainties (relative to NmE without modification of input parameters) are in the range of 60%–95%. Similar to Knight et al. (2018), who compared NmE derived from SUSSI LBH measurements with NmE of high latitude digisonde measurements, precipitation NmE and ISR NmE show modest agreement in Figure 12. They are not statistically correlated, however, with a Pearson correlation coefficient of 0.52.

Figure 12b is the hmE uncertainty as a function of SSUSI/GUVI  $E_0$ , which is the primary factor in determining the altitude of the enhanced ionization layer. Small dots show results for each individual ISR-UVI conjunctions and large dots are binned averages. Uncertainty in UVI  $E_0$  inputs are the dominant factor in hmE uncertainty, which increases with UVI  $E_0$  at lower  $E_0$  values up to  $\sim 22 \text{ km}$  at 7 keV, and gradually decreases with  $E_0$  for higher energies as the ionization layer narrows in the lower ionosphere. Uncertainties due to spectral shape are also significant at lower energies when the precipitation layer is at higher altitudes, peaking at 11 km at 3 keV and decreasing gradually with energy. Cumulative uncertainties follow roughly the same pattern as those due to  $E_0$  uncertainties, peaking at  $\sim 26 \text{ km}$  at 7 keV. Likely due to the large hmE uncertainties of precipitation-enhanced densities, there is no correlation between UVI and ISR hmE in Figure 13. Results of Knight et al. (2018) also showed no agreement between SSUSI LBH hmE and digisonde hmE values.

## 5. Discussion and Ongoing Work

As demonstrated in Section 3, E-CHAIM's auroral region performance below 200 km altitude is substantially improved with the addition of a SSUSI/GUVI-based precipitation component. Improvements are often a few orders of magnitude during winter and equinox seasons. However, there remains substantial room for further improvement given lingering OOM underestimates of ISR measurements by precipitation-enhanced densities during low AE periods, some tendency for precipitation-enhanced densities to overshoot those of ISR measurements, particularly in the E-region, and an inability to accurately capture NmE and hmE of enhanced E-layers. Some of these deficiencies may be a result of the large uncertainties associated with the precipitation scheme.

As demonstrated in Section 4, the primary error sources for precipitation-enhanced densities are uncertainties in SUSSI/GUVI  $E_0$  and  $Q_0$  data and the choice of distribution function for precipitation energy spectrum. Uncertainties in the E-CHAIM model used for the background ionization of the precipitation-enhanced density will also contribute to deviations from ISR measurements and could be a factor in some of the lower ionosphere discrepancies observed during low AE intervals when UVI  $Q_0$  tends to be low. E-CHAIM errors will play less of a role in high  $Q_0$  situations when the precipitation component dominates at low altitudes <200 km.

In arriving at Equation 6 from the continuity equation for ionosphere density, it was necessary to neglect time dependence and assume a steady state. This is a necessary assumption since E-CHAIM is an empirical model that generates an instantaneous 3D representation of ionospheric electron density and as such does not accommodate time dependence. As discussed in Semeter and Kamalabadi (2005), the steady-state assumption is valid when the response time of the ionosphere is smaller than the time scales over which significant variability in electron precipitation is observed. Ionospheric response times can be <1 second up

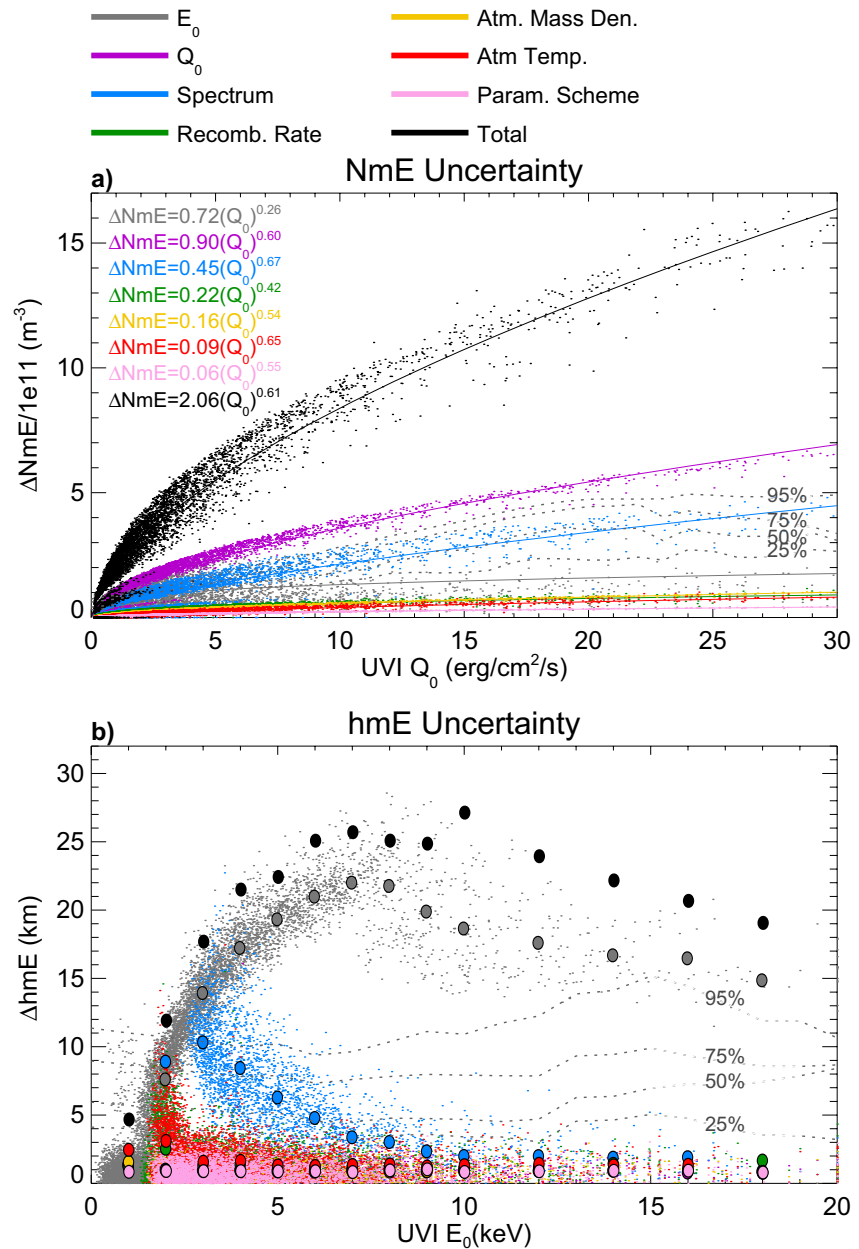


**Figure 12.** Sensitivity of Empirical Canadian High Arctic Ionospheric Model + precipitation component (a) NmE and (b) hmE to uncertainties of parameterization scheme input parameters (color coded), along with cumulative sensitivity (in black). Small dots are sensitivities for each individual conjunction. Lines in (a) are power law fits, and large dots in (b) are binned averages. ISR, incoherent scatter radar; UVI, ultraviolet image.

to 10s of seconds depending on the ionosphere density (Figure 3 in Semeter & Kamalabadi, 2005), and thus there will be cases where the precipitation flux varies on time scales smaller than the ionospheric response time. In these cases, the steady state assumption will inevitably produce errors in calculated precipitation-enhanced densities.

An additional source of error may be the precipitation of energetic protons into the auroral ionosphere, the effects of which are removed from SSUSI and GUVI  $E_0$  and  $Q_0$  data products. According to Newell et al. (2009), DMSP particle sensors have observed significant auroral ion precipitation across late afternoon/evening and early morning sectors at auroral ISR latitudes, which may contribute to some of the precipitation scheme underestimation of ISR densities. In addition, Knight et al. (2018) predicted that

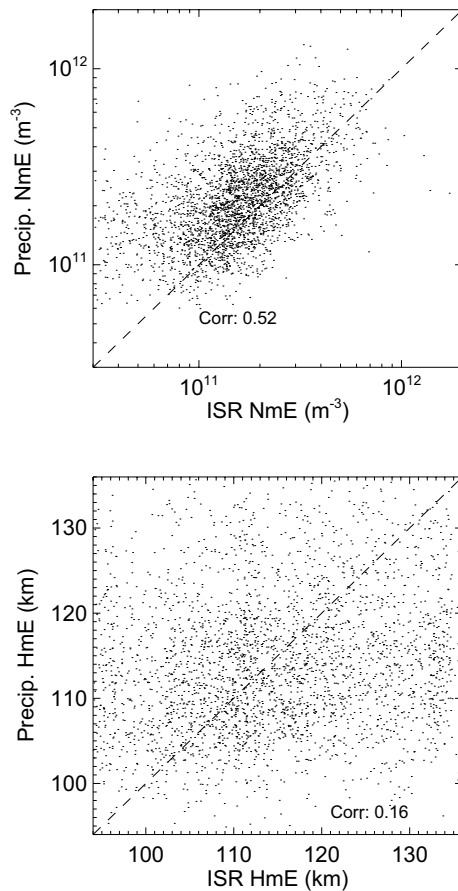


**Figure 13.** (a) NmE and (b) hme of Empirical Canadian High Arctic Ionospheric Model + precipitation component density profiles versus incoherent scatter radar (ISR) density profiles, for all ISR-UVI conjunctions. Pearson correlation coefficients are shown in each figure. Dashed lines are drawn as a guide to ideal correlation.

satellite LBH-derived NmE may be biased by up to 20% in the presence of proton precipitation (if assuming only electron precipitation), however Knight (2019) found no such bias when comparing LBH-derived NmE with NmE of ionosonde radars. To potentially account for ion precipitation contributions and as an aid to electron precipitation contributions, we plan on testing the OVATION-Prime Model (Newell et al., 2014), an empirical model for auroral ion and electron precipitation characteristics based on DMSP SSJ data, to support UVI inputs to the precipitation scheme for E-CHAIM. Statistical comparison of DMSP SSJ particle data and SSUSI data may also provide an additional constraint for precipitation scheme inputs. We are also working on a method to integrate optimal spectral shape into the precipitation scheme. This may involve a climatological model to describe ideal spectrum based on AE index and local time, as in Figure 9.

## 6. Conclusions

We have used satellite-based UVI imager data (DMSP SSUSI and TIMED GUVI) and the Fang-2010 parameterization of atmospheric ionization rates to develop a precipitation enhanced density component for the E-CHAIM model at high latitudes. Precipitation enhanced densities were tested by comparison with ISR ionosphere density measurements during conjunctions between ISR and satellite UVI fields of view. Twenty-nine thousand and thirty-eight such conjunctions from 2005 to 2019 have revealed substantial improvements in E-CHAIM's representation of auroral region densities at altitudes of 90–200 km with inclusion of the precipitation component, where the RMS difference between E-CHAIM and ISR measurements decreased by up to  $2.9 \times 10^{10}$  ele/m<sup>3</sup>. Largest improvements were observed in the E-region ionosphere. Minor improvements were also observed in the polar cap after inclusion of the precipitation component, where the RMS difference between E-CHAIM and ISR measurements decreased by up to  $2.6 \times 10^9$  ele/m<sup>3</sup>. Improvements were most substantial, often multiple orders of magnitude, during active auroral periods, and during the winter season. E-CHAIM precipitation enhanced densities show best agreement with ISR measurements in the

afternoon-evening sector, with a tendency to underestimate ISR densities in the morning sector. These morning sector underestimations are characterized by enhanced E-region densities in ISR measurements, but no substantial  $Q_0$  in the corresponding UVI data, and mainly occurred during quiet auroral intervals.

To determine the main potential sources of error in the precipitation component, the sensitivity of precipitation-enhanced densities to uncertainties in input parameters was also tested. Precipitation enhanced densities were most sensitive to uncertainties associated with UVI  $E_0$ , UVI  $Q_0$ , and the choice of energy distribution function for precipitating electrons. Estimated total uncertainties in precipitation-enhanced densities were less than  $1 \times 10^{11}$  ele/m<sup>3</sup> for  $Q_0 < 2$  erg/cm<sup>2</sup>/s and as large as  $6 \times 10^{11}$  ele/m<sup>3</sup> for  $Q_0 > 10$  erg/cm<sup>2</sup>/s, and generally increased with  $Q_0$  and with decreasing altitude. Methods of applying the empirical Ovation-PRIME model and DMSP SSJ particle data to constrain  $E_0$  and  $Q_0$  inputs are being investigated, while a climatological model for ideal energy distribution function is also being developed. The precipitation scheme has been implemented into the E-CHAIM model as part of the E-CHAIM v3.0 software update, and is freely available at <https://chain-new.chain-project.net/index.php/chain/e-chain> (with the creation of a free account). A paper describing this implementation is forthcoming.

## Data Availability Statement

Software for the E-CHAIM model is available at <https://chain-new.chain-project.net/index.php/chaim/e-chaim>. SSUSI Auroral EDR data used in this study are version 106, revision 0, and are available at <https://ssusi.jhuapl.edu/>. GUVI EDR Aurora data used in this study are version 106, revision 1, and are available at <http://guvitimed.jhuapl.edu/>. ISR data used in this study were acquired from the Madrigal database at <http://millstonehill.haystack.mit.edu/>. The NRLMSISE-00 atmosphere model is available at <https://ccmc.gsfc.nasa.gov/modelweb/models/nrlmsise00.php>. The IRI-2016 model is available at [https://ccmc.gsfc.nasa.gov/modelweb/models/iri2016\\_vitmo.php](https://ccmc.gsfc.nasa.gov/modelweb/models/iri2016_vitmo.php). Auroral electrojet (AE) indices are from the OMNI database (<https://cdaweb.gsfc.nasa.gov/index.html/>). DMSP SSJ particle data are from the National Oceanic and Atmospheric Administration (NOAA) National Centers for Environmental Information (NCEI) space weather service (<https://www.ngdc.noaa.gov/stp/satellite/dmsp/>).

## Acknowledgments

Funding for this study was provided by Defence Research and Development Canada (DRDC), the National Science and Engineering Research Council (NSERC), and the Canadian Space Agency (CSA). The authors would like to thank all ISR operators for their continued contribution of data to the Madrigal Database.

## References

- Aksnes, A., Stadsnes, J., Østgaard, N., Germany, G. A., Oksavik, K., Vondrak, R. R., et al. (2006). Height profiles of the ionospheric electron density derived using space-based remote sensing of UV and X ray emissions and EISCAT radar data: A ground-truth experiment. *Journal of Geophysical Research*, *111*, A02301. <https://doi.org/10.1029/2005ja011331>
- Bilitza, D., Altadill, D., Truhlik, V., Shubin, V., Galkin, I., Reinisch, B., & Huang, X. (2017). International Reference Ionosphere 2016: From ionospheric climate to real-time weather predictions. *Space Weather*, *15*, 418–429. <https://doi.org/10.1002/2016sw001593>
- Evans, J. V. (1969). Theory and practice of ionosphere study by Thomson scatter radar. *Proceedings of the IEEE*, *57*(4), 496–530. <https://doi.org/10.1109/PROC.1969.7005>
- Fang, X., Randall, C. E., Lummerzheim, D., Wang, W., Lu, G., Solomon, S. C., & Frahm, R. A. (2010). Parameterization of monoenergetic electron impact ionization. *Geophysical Research Letters*, *37*, L22106. <https://doi.org/10.1029/2010gl045406>
- Germany, G. A., Parks, G. K., Brittnacher, M., Cumnock, J., Lummerzheim, D., Spann, J. F., et al. (1997). Remote determination of auroral energy characteristics during substorm activity. *Geophysical Research Letters*, *24*(8), 995–998. <https://doi.org/10.1029/97GL00864>
- Germany, G. A., Torr, M. R., Richards, P. G., & Torr, D. G. (1990). The dependence of modeled OI 1356 and N<sub>2</sub> Lyman Birge Hopfield auroral emissions on the neutral atmosphere. *Journal of Geophysical Research*, *95*(A6), 7725–7733. <https://doi.org/10.1029/ja095ia06p07725>
- Gledhill, J. A. (1986). The effective recombination coefficient of electrons in the ionosphere between 50 and 150 km. *Radio Science*, *21*(3), 399–408. <https://doi.org/10.1029/rs021i003p00399>
- Hernández-Pajares, M., Juan, J. M., Sanz, J., & Colombo, O. L. (2002). Improving the real-time ionospheric determination from GPS sites at very long distances over the equator. *Journal of Geophysical Research*, *107*(A10), 1296. <https://doi.org/10.1029/2001JA009203>
- Humm, D. C., Paxton, L. J., Christensen, A. B., Ogorzalek, B. S., Pardoe, C. T., Meng, C.-I., et al. (1998). Design and performance of the Global Ultraviolet Imager (GUUVI) (Vol. 3445, pp. 2–12). *Proceedings of SPIE, EUV, X-Ray, and Gamma-Ray Instrumentation for Astronomy IX*. <https://doi.org/10.1117/12.330325>
- Jodalen, V., Bergsvik, T., Cannon, P. S., & Arthur, P. C. (2001). Performance of HF modems on high-latitude paths using multiple frequencies. *Radio Science*, *36*(6), 1687–1698. <https://doi.org/10.1029/2000rs002547>
- Khazanov, G. V., Glocer, A., & Himwich, E. W. (2014). Magnetosphere-ionosphere energy interchange in the electron diffuse aurora. *Journal of Geophysical Research: Space Physics*, *119*, 171–184. <https://doi.org/10.1002/2013ja019325>
- Kletzing, C. A., Scudder, J. D., Dors, E. E., & Curto, C. (2003). Auroral source region: Plasma properties of the high-latitude plasma sheet. *Journal of Geophysical Research*, *108*, 1360. <https://doi.org/10.1029/2002ja009678>
- Knight, H. K. (2019). Auroral ionospheric E region parameters obtained from satellite-based far ultraviolet and ground-based ionosonde observations: Effects of proton precipitation. *Annales Geophysicae*, *39*(1), 105–118. <https://doi.org/10.5194/angeo-2019-110>
- Knight, H. K., Galkin, I. A., Reinisch, B. W., & Zhang, Y. (2018). Auroral ionospheric E region parameters obtained from satellite-based far ultraviolet and ground-based ionosonde observations: Data, methods, and comparisons. *Journal of Geophysical Research: Space Physics*, *123*, 6065–6089. <https://doi.org/10.1029/2017ja024822>
- Lummerzheim, D. (1992). *Comparison of energy dissipation functions for high energy auroral electrons and ion precipitation* (Report UAG-R-318). Geophysical Institute, University of Alaska-Fairbanks.
- Lummerzheim, D., Rees, M. H., Craven, J. D., & Frank, L. A. (1991). Ionospheric conductances derived from DE-1 auroral images. *Journal of Atmospheric and Terrestrial Physics*, *53*(3–4), 281–292. [https://doi.org/10.1016/0021-9169\(91\)90112-K](https://doi.org/10.1016/0021-9169(91)90112-K)
- Maltseva, O. A., & Nikitenko, T. V. (2020). Validation of various ionospheric models in the high-latitude zone. *Advances in Space Research*. <https://doi.org/10.1016/j.asr.2020.09.016>
- Mathews, J. D. (1984). The incoherent scatter radar as a tool for studying the ionospheric D-region. *Journal of Atmospheric and Terrestrial Physics*, *46*(11), 975–986. [https://doi.org/10.1016/0021-9169\(84\)90004-7](https://doi.org/10.1016/0021-9169(84)90004-7)
- McIntosh, R. C., & Anderson, P. C. (2014). Maps of precipitating electron spectra characterized by Maxwellian and kappa distributions. *Journal of Geophysical Research: Space Physics*, *119*, 10116–10132. <https://doi.org/10.1002/2014ja020080>
- Newell, P. T., Liou, K., Zhang, Y., Sotirelis, T., Paxton, L. J., & Mitchell, E. J. (2014). OVATION Prime-2013: Extension of auroral precipitation model to higher disturbance levels. *Space Weather*, *12*, 368–379. <https://doi.org/10.1002/2014SW001056>
- Newell, P. T., Sotirelis, T., & Wing, S. (2009). Diffuse, monoenergetic, and broadband aurora: The global precipitation budget. *Journal of Geophysical Research*, *114*, A09207. <https://doi.org/10.1029/2009ja014326>
- Paxton, L. J., Meng, C.-I., Fountain, G. H., Ogorzalek, B. S., Darlington, E. H., Gary, S. A., et al. (1992). Special sensor ultraviolet spectrographic imager: An instrument description (Vol. 1745). SPIE Proceedings Instrumentation for Planetary and Terrestrial Atmospheric Remote Sensing. <https://doi.org/10.1117/12.60595>
- Perez-Ruiz, M., & Upadhyaya, S. K. (2012). GNSS in precision agricultural operations. In F. B. Elbahhar & A. Rivenq (Eds.), *New approach of indoor and outdoor localization systems*. Tech Europe. <https://doi.org/10.5772/50448>
- Picone, J. M., Hedin, A. E., Drob, D. P., & Aikin, A. C. (2002). NRLMSISE-00 empirical model of the atmosphere: Statistical comparisons and scientific issues. *Journal of Geophysical Research*, *107*(A12), 1468. <https://doi.org/10.1029/2002JA009430>

- Redmon, R. J., Denig, W. F., Kilcommons, L. M., & Knipp, D. J. (2017). New DMSP database of precipitating auroral electrons and ions. *Journal of Geophysical Research: Space Physics*, *122*, 9056–9067. <https://doi.org/10.1002/2016ja023339>
- Rees, M. H. (1963). Auroral ionization and excitation by incident energetic electrons. *Planetary and Space Science*, *11*, 1209–1218. [https://doi.org/10.1016/0032-0633\(63\)90252-6](https://doi.org/10.1016/0032-0633(63)90252-6)
- Roble, R. G., & Ridley, E. C. (1987). An auroral model for the NCAR thermospheric general circulation model (TGCM). *Annales Geophysicae*, *5A*, 369–382.
- Schunk, R., & Nagy, A. (2009). *Ionospheres: Physics, plasma physics, and chemistry* (2nd ed.). Cambridge University Press. <https://doi.org/10.1017/CBO9780511635342>
- Semeter, J., & Kamalabadi, F. (2005). Determination of primary electron spectra from incoherent scatter radar measurements of the auroral E region. *Radio Science*, *40*, RS2006. <https://doi.org/10.1029/2004RS003042>
- Sheehan, C. H., & St. Maurice, J.-P. (2004). Dissociative recombination of  $N_2^+$ ,  $O_2^+$ , and  $NO^+$ : Rate coefficients for ground state and vibrationally excited ions. *Journal of Geophysical Research*, *109*, A03302. <https://doi.org/10.1029/2003ja010132>
- Sládková, D., Kapica, R., & Vrabel, M. (2011). Global navigation satellite system (GNSS) technology for automation of surface mining. *International Journal of Mining, Reclamation and Environment*, *25*(3), 284–294. <https://doi.org/10.1080/17480930.2011.608879>
- Sotirelis, T., Korth, H., Hsieh, S.-Y., Zhang, Y., Morrison, D., & Paxton, L. (2013). Empirical relationship between electron precipitation and far-ultraviolet auroral emissions from DMSP observations. *Journal of Geophysical Research: Space Physics*, *118*, 1203–1209. <https://doi.org/10.1002/jgra.50157>
- Strickland, D. J., Book, D. L., Coffey, T. P., & Fedder, J. A. (1976). Transport equation techniques for the deposition of auroral electrons. *Journal of Geophysical Research*, *81*(16), 2755–2764. <https://doi.org/10.1029/ja081i016p02755>
- Strickland, D. J., Evans, J. S., & Paxton, L. J. (1995). Satellite remote sensing of thermospheric  $O/N_2$  and solar EUV: 1. Theory. *Journal of Geophysical Research*, *100*(A7), 12217–12226. <https://doi.org/10.1029/95JA00574>
- Strickland, D. J., Jasperse, J. R., & Whalen, J. A. (1983). Dependence of auroral FUV emissions on the incident electron spectrum and neutral atmosphere. *Journal of Geophysical Research*, *88*(A10), 8051–8062. <https://doi.org/10.1029/ja088ia10p08051>
- Themens, D. R., Jayachandran, P. T., Bilitza, D., Erickson, P. J., Häggström, I., Lyashenko, M. V., et al. (2018). Topside electron density representations for middle and high latitudes: A topside parameterization for E-CHAIM based on the NeQuick. *Journal of Geophysical Research: Space Physics*, *123*, 1603–1617. <https://doi.org/10.1002/2017JA024817>
- Themens, D. R., Jayachandran, P. T., Galkin, I., & Hall, C. (2017). The Empirical Canadian High Arctic Ionospheric Model (E-CHAIM):  $N_mF_2$  and  $h_mF_2$ . *Journal of Geophysical Research: Space Physics*, *122*, 9015–9031. <https://doi.org/10.1002/2017JA024398>
- Themens, D. R., Jayachandran, P. T., & McCaffrey, A. M. (2019). Validating the performance of the Empirical Canadian High Arctic Ionospheric Model (E-CHAIM) with in situ observations from DMSP and CHAMP. *Journal of Space Weather and Space Climate*, *9*, A21. <https://doi.org/10.1051/swsc/2019021>
- Themens, D. R., Jayachandran, P. T., McCaffrey, A. M., Reid, B., & Varney, R. H. (2019). A bottomside parameterization for the Empirical Canadian High Arctic Ionospheric Model (E-CHAIM). *Radio Science*, *54*, 397–414. <https://doi.org/10.1029/2018RS006748>
- Themens, D. R., Jayachandran, P. T., Reid, B., & McCaffrey, A. M. (2020). The limits of empirical electron density modeling: Examining the capacity of E-CHAIM and the IRI for modeling intermediate (1- to 30-day) timescales at high latitudes. *Radio Science*, *55*. <https://doi.org/10.1029/2018rs006763>
- Vickrey, J. F., Vondrak, R. R., & Matthews, S. J. (1982). Energy deposition by precipitating particles and Joule dissipation in the auroral ionosphere. *Journal of Geophysical Research*, *87*(A7), 5184–5196. <https://doi.org/10.1029/ja087ia07p05184>
- Xiong, C., & Lühr, H. (2014). An empirical model of the auroral oval derived from CHAMP field-aligned current signatures—Part 2. *Annales Geophysicae*, *32*, 623–631. <https://doi.org/10.5194/angeo-32-623-2014>
- Yue, X., Schreiner, W. S., Lei, J., Sokolovskiy, S. V., Rocken, C., Hunt, D. C., & Kuo, Y.-H. (2010). Error analysis of Abel retrieved electron density profiles from radio occultation measurements. *Annales Geophysicae*, *28*, 217–222. <https://doi.org/10.5194/angeo-28-217-2010>
- Zaalov, N. Y., Warrington, E. M., & Stocker, A. J. (2003). Simulation of off-great circle HF propagation effects due to the presence of patches and arcs of enhanced electron density within the polar cap ionosphere. *Radio Science*, *38*, 1052. <https://doi.org/10.1029/2002RS002798>
- Zhang, Y., Paxton, L. J., Bilitza, D., & Doe, R. (2010). Real-time assimilation in IRI of auroral peak E-region density and equatorward boundary. *Advances in Space Research*, *46*, 1055–1063. <https://doi.org/10.1016/j.asr.2010.06.029>